Article

Cell Reports

Surface-Matrix Screening Identifies Semi-specific Interactions that Improve Potency of a Near Pan-reactive HIV-1-Neutralizing Antibody

Graphical Abstract

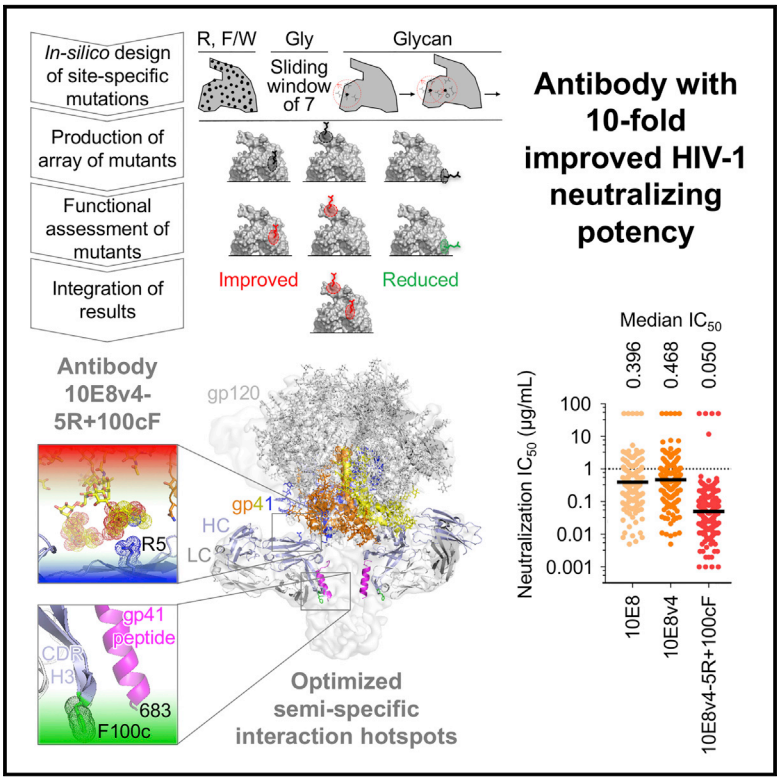

Highlights

- Development of a surface-matrix screening approach to improve antibody function
- Identified hydrophobic mutations that improved 10E8 interaction with HIV-1 membrane
- Identified positively charged mutations that improved interactions with HIV-1 glycan
- Optimizing semi-specific interactions can improve potency while maintaining breadth

Authors

Young D. Kwon, Gwo-Yu Chuang, Baoshan Zhang, ..., Lawrence Shapiro, John R. Mascola, Peter D. Kwong

Correspondence

jmascola@nih.gov (J.R.M.), pdkwong@nih.gov (P.D.K.)

In Brief

Antibodies could impact the treatment and prevention of HIV-1 if they were sufficiently potent to allow cost-effective delivery. Kwon et al. used a surface-matrix screening approach to improve the potency of antibody 10E8 by ~10-fold. The improved antibody, 10E8v4-5R+100cF, has among the best breadth and potency of current HIV-1-neutralizing antibodies.

Data and Software Availability

5WDF

Kwon et al., 2018, Cell Reports *22*, 1798–1809
February 13, 2018
https://doi.org/10.1016/j.celrep.2018.01.023

CellPress

OPEN ACCESS
CellPress

Cell Reports
Article

Surface-Matrix Screening Identifies Semi-specific Interactions that Improve Potency of a Near Pan-reactive HIV-1-Neutralizing Antibody

Young D. Kwon,[1,7] Gwo-Yu Chuang,[1,7] Baoshan Zhang,[1,7] Robert T. Bailer,[1] Nicole A. Doria-Rose,[1] Tatyana S. Gindin,[2] Bob Lin,[1] Mark K. Louder,[1] Krisha McKee,[1] Sijy O'Dell,[1] Amarendra Pegu,[1] Stephen D. Schmidt,[1] Mangaiarkarasi Asokan,[1] Xuejun Chen,[1] Misook Choe,[1] Ivelin S. Georgiev,[1] Vivian Jin,[1] Marie Pancera,[1] Reda Rawi,[1] Keyun Wang,[1] Rajoshi Chaudhuri,[1] Lisa A. Kueltzo,[1] Slobodanka D. Manceva,[1] John-Paul Todd,[1] Diana G. Scorpio,[1] Mikyung Kim,[3] Ellis L. Reinherz,[3] Kshitij Wagh,[4] Bette M. Korber,[4] Mark Connors,[5] Lawrence Shapiro,[6] John R. Mascola,[1,*] and Peter D. Kwong[1,6,8,*]

[1]Vaccine Research Center, National Institute of Allergy and Infectious Diseases (NIAID), NIH, Bethesda, MD 20892, USA
[2]Department of Pathology and Cell Biology, Columbia University, New York, NY 10032, USA
[3]Dana-Farber Cancer Institute, Harvard Medical School, Boston, MA 02215, USA
[4]Los Alamos National Laboratory, Los Alamos, NM 87545, USA
[5]Laboratory of Immunoregulation, National Institute of Allergy and Infectious Diseases, NIH, Bethesda, MD 20892, USA
[6]Department of Biochemistry and Molecular Biophysics, Columbia University, New York, NY 10032, USA
[7]These authors contributed equally
[8]Lead Contact
*Correspondence: jmascola@nih.gov (J.R.M.), pdkwong@nih.gov (P.D.K.)
https://doi.org/10.1016/j.celrep.2018.01.023

SUMMARY

Highly effective HIV-1-neutralizing antibodies could have utility in the prevention or treatment of HIV-1 infection. To improve the potency of 10E8, an antibody capable of near pan-HIV-1 neutralization, we engineered 10E8-surface mutants and screened for improved neutralization. Variants with the largest functional enhancements involved the addition of hydrophobic or positively charged residues, which were positioned to interact with viral membrane lipids or viral glycan-sialic acids, respectively. In both cases, the site of improvement was spatially separated from the region of antibody mediating molecular contact with the protein component of the antigen, thereby improving peripheral semi-specific interactions while maintaining unmodified dominant contacts responsible for broad recognition. The optimized 10E8 antibody, with mutations to phenylalanine and arginine, retained the extraordinary breadth of 10E8 but with ~10-fold increased potency. We propose surface-matrix screening as a general method to improve antibodies, with improved semi-specific interactions between antibody and antigen enabling increased potency without compromising breadth.

INTRODUCTION

With antibody-based therapeutics dominating the biologics pipelines of leading pharmaceutical companies (Ayyar et al., 2016; Chames et al., 2009), methods to improve antibody functionality have been eagerly sought. The payoffs are clear: if antibody efficacy were to increase 10-fold, the amount of delivered antibody required to achieve efficacy might decrease 10-fold, with concomitant decreases in dosing, side effects, and/or costs. Whereas optimization of small-molecule therapeutics is well established, many biologics are utilized as identified by functional screening, without substantial optimization of therapeutic functionality. Indeed, while specific antibody constant-region mutations have been identified for increasing antibody half-life (Roopenian and Akilesh, 2007) or for reducing reactivity (for example, by humanization for non-human antibodies) (Hwang and Foote, 2005), it has been a challenge to improve antibody therapeutic functionality by *in vitro* optimization. For example, attempts to improve palivizumab (Synagis), the sole monoclonal antibody licensed for an infectious disease (respiratory syncytial virus infection), have met with difficulty, with standard methods for optimizing protein interactions such as phage display showing uncertain translation to *in vivo* therapeutic efficacy (Ramilo et al., 2014; Wu et al., 2007).

In the case of HIV-1, potent broadly neutralizing antibodies have been sought as therapeutics or for prevention. A cocktail of five antibodies has shown therapeutic potential in animal studies (Klein et al., 2012), and antibodies such as 3BNC117, VRC01, and members of the PGT121 family are showing promise in clinical studies (Bar et al., 2016; Caskey et al., 2015, 2017; Scheid et al., 2016; Schoofs et al., 2016). VRC01, a human antibody identified from an HIV-1-infected donor, is capable of neutralizing over 90% of HIV-1, with a median 50% inhibitory concentration (IC_{50}) of 0.33 μg/mL (Wu et al., 2010), and its preventive efficacy is currently being assessed in a Phase IIb prevention study, with dosing up to ~2 g VRC01 every 2 months for an average adult. At this dosing, long-term use of antibody VRC01 would likely be impractical; however, only ~0.2 g every 2 months might be required for an antibody 10-fold more potent than VRC01, easing issues of practicality.

To improve antibody effectiveness, structure-based design and other hypothesis-based deductive approaches have been undertaken. For example, with antibodies of the VRC01 class (Zhou et al., 2013), antibody NIH45-46 could be significantly improved by a G54W mutation, designed to mimic the recognition of the CD4 receptor (Diskin et al., 2011; Scheid et al., 2011). Unfortunately, the NIH45-46 G54W variant proved to be polyreactive. However, a combination approach succeeded in obtaining VRC07-523LS, an improved VRC01-class antibody containing multiple sequence alterations and displaying increased potency and tolerable polyreactivity (Rudicell et al., 2014). Importantly, the VRC07-523LS antibody required only one-fifth the dose to achieve the same protection as VRC01 in rhesus macaques (Rudicell et al., 2014).

While deductive approaches (Figure 1A, left) can improve antibody functionality, such approaches can only be used with characterized interactions. Here, we sought to test a surface matrix-screening approach (Figure 1A, right) that used virus neutralization as the target readout, incorporated chemical alterations of surface residues, and assessed and integrated the desired properties. We chose antibody 10E8 for improvement, due to its ability to neutralize >97% of HIV strains, with a median IC_{50} potency of 0.40 μg/mL by recognizing the membrane-proximal external region (MPER) of the HIV-1 envelope (Env) (Huang et al., 2012). We identified single amino-acid mutations that improved neutralization potency and analyzed the chemical preferences of each functional hotspot to reveal mechanistic insights. Identified hotspots were distinct from the region of the antibody mediating molecular contact with the protein component of the antigen and appeared to enhance semi-specific interactions with either the glycan shield or the viral membrane. Notably, the optimized 10E8 antibody, displayed a median IC_{50} of 0.050 μg/mL, about 2-fold lower than that of antibody N6 (Huang et al., 2016a), a recently described broadly neutralizing antibody targeting the CD4-binding site of HIV-1, which is one of the most potent broadly neutralizing antibodies discovered thus far. Remarkably, the combination of the improved 10E8v4-5R+100cF variant with N6 neutralized all HIV-1 strains in our 208-isolate panel, at less than 1 μg/mL, with a median IC_{50} of 0.016 μg/mL.

RESULTS

Surface-Matrix Screening of Antibody 10E8

For alterations of surface chemistry, we chose types of residue substitutions observed in other cases to improve antibody functionality (Figure 1B). We chose Phe (or Trp, if the wild-type residue was Phe or Tyr), as hydrophobic interactions are common in antibody-antigen recognition (Diskin et al., 2011; Young et al., 1994). We also chose Arg, which can improve solubility, can mediate interactions with phospholipid membranes, or can interfere with antigen interactions through steric clashes (Gorman et al., 2016; McLellan et al., 2011; Robison et al., 2016; Trevino et al., 2007). To assess the effects of amino-acid side-chain removal, we tested substitutions of outwardly facing residues to glycine in windows of 7 residues (2 overlapping). Lastly, we tested the effects of introducing N-linked glycans on the antibody surface, as glycans are hydrophilic, with the potential to increase solubility (Hebert et al., 2014), to introduce steric clashes at sites of interaction and to enhance potency in select cases (Song et al., 2013).

Starting with 10E8, we used the crystal structure (Huang et al., 2012) of the antigen-binding fragment (Fab) to calculate the solvent accessibility of each amino-acid residue. For each residue with greater than 30% solvent accessibility, we produced single point mutants: 105 Phe (or Trp) mutants and 98 Arg mutants. We also produced 48 7-Gly mutants and 47 *N*-glycan variants (Figure S1; Tables S1A and S1B). In total, we created 298 10E8 variants, each of which we synthesized and expressed.

To assess the impact of each mutation on neutralization, we tested a nine-virus panel, selected to cover a range of potencies and diverse clades (Figure 1C). Assessment of wild-type 10E8 neutralization indicated substantial variation in replicated measurements, ranging from geometric SDs of 1.3 (for strain ZM106.9) to 5.6 (for strain KER2008.12); we proceeded with the five isolates that showed the least replicate variation (Figure 1D). With an error in potency of 1.5-fold, we estimated that assessment of 298 variants should allow for the identification of variants with as little as ~2-fold improvement in potency (Figure 1E; Figure S2).

Two variants showed improvements of over 2.5-fold in potency (Figure 1F; Table S1C). One mutation, $S100cF_{HC}$ (we use Kabat nomenclature for antibody numbering, with residue 100c being the third residue after 100a and subscripts HC and LC to represent heavy and light chains, respectively), increased neutralization potency by almost 4-fold, and a second mutation, $V5R_{HC}$, increased neutralization potency by just under 3-fold. (Figure 1F). To understand the impact of $Arg5_{HC}$ and $Phe100c_{HC}$ mutations on the structure of 10E8, we added these mutations to antibody 10E8v4 (Kwon et al., 2016), a solubility-improved variant with breadth and neutralization potency similar to those of 10E8, and crystallized the antigen-binding fragment (Fab) of 10E8v4-5R+100cF in complex with a 19-mer peptide encompassing its MPER epitope. Diffraction data extended to 3.1 Å resolution, and structure solution by molecular replacement and refinement yielded an R_{work}/R_{free} of 0.24/0.28 (Table S2). Overall, the structure revealed both $Arg5_{HC}$ and $Phe100c_{HC}$ mutations to minimally alter the Fab structure and to be distal from one another and peripheral to the main contacts between MPER and 10E8 (Figure 1G).

Delineation of 10E8 Functional Surfaces by Surface-Matrix Screening

Multiple variants showed reductions in neutralization of over 3 SDs (Figure S1, right panels; Table S1C). Many of these deleterious mutations involved the introduction of bulky moieties that could sterically inhibit binding, while others involved substitutions of critical paratope residues. The observed deleterious mutations clustered in coherent patterns to selected surfaces (Figure 2A). To provide biological context, we evaluated these surfaces in the context of the cryoelectron microscopy (cryo-EM) structure of the detergent-solubilized Env trimer bound by antibodies PGT151 and 10E8 (Lee et al., 2016) (Figure 2B). Notably, in addition to epitope-contacting residues, two surfaces—one facing the expected location of the Env trimer and the other facing the expected location of the viral membrane—were identified by clusters of inhibitory mutations.

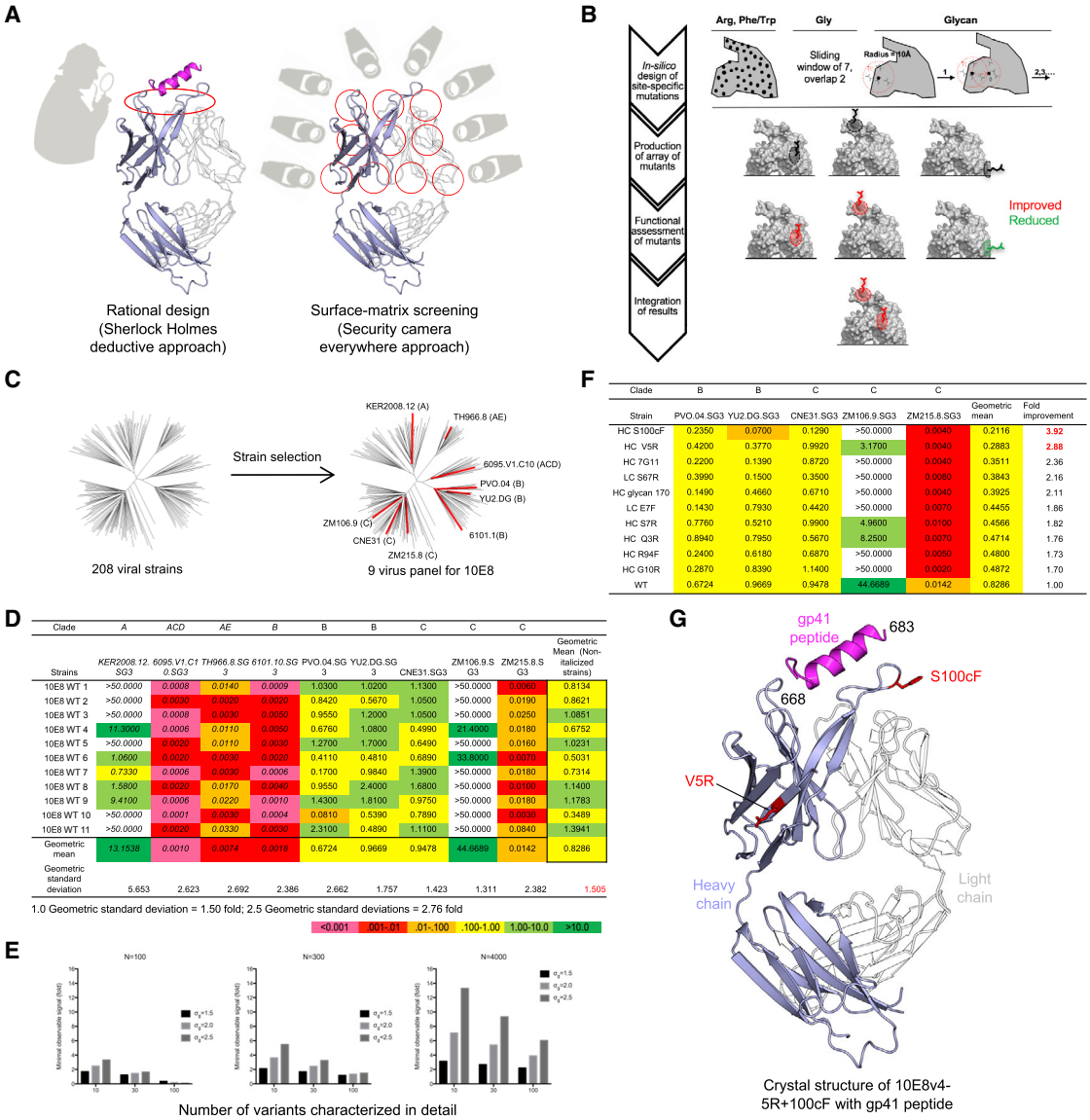

Clade	B	B	C	C	C		
Strain	PVO.04.SG3	YU2.DG.SG3	CNE31.SG3	ZM106.9.SG3	ZM215.8.SG3	Geometric mean	Fold improvement
HC S100cF	0.2350	0.0700	0.1290	>50.0000	0.0040	0.2116	3.92
HC V5R	0.4200	0.3770	0.9920	3.1700	0.0040	0.2883	2.88
HC 7G11	0.2200	0.1390	0.8720	>50.0000	0.0040	0.3511	2.36
LC S67R	0.3990	0.1500	0.3500	>50.0000	0.0080	0.3843	2.16
HC glycan 170	0.1490	0.4660	0.6710	>50.0000	0.0040	0.3925	2.11
LC E7F	0.1430	0.7930	0.4420	>50.0000	0.0070	0.4455	1.86
HC S7R	0.7760	0.5210	0.9900	4.9600	0.0100	0.4566	1.82
HC Q3R	0.8940	0.7950	0.5670	8.2500	0.0070	0.4714	1.76
HC R94F	0.2400	0.6180	0.6870	>50.0000	0.0050	0.4800	1.73
HC G10R	0.2870	0.8390	1.1400	>50.0000	0.0020	0.4872	1.70
WT	0.6724	0.9669	0.9478	44.6689	0.0142	0.8286	1.00

Clade	A	ACD	AE	B	B	B	C	C	C	
Strains	KER2008.12. SG3	6095.V1.C1 0.SG3	TH966.8.SG 3	6101.10.SG 3	PVO.04.SG 3	YU2.DG.SG 3	CNE31.SG3	ZM106.9.S G3	ZM215.8.S G3	Geometric Mean (Non-italicized strains)
10E8 WT 1	>50.0000	0.0008	0.0140	0.0009	1.0300	1.0200	1.1300	>50.0000	0.0060	0.8134
10E8 WT 2	>50.0000	0.0030	0.0020	0.0020	0.8420	0.5670	1.0500	>50.0000	0.0190	0.8621
10E8 WT 3	>50.0000	0.0008	0.0030	0.0050	0.9550	1.2000	1.0500	>50.0000	0.0250	1.0851
10E8 WT 4	11.3000	0.0006	0.0110	0.0050	0.6760	1.0800	0.4990	21.4000	0.0180	0.6752
10E8 WT 5	>50.0000	0.0020	0.0110	0.0030	1.2700	1.7000	0.6490	>50.0000	0.0160	1.0231
10E8 WT 6	1.0600	0.0020	0.0030	0.0020	0.4110	0.4810	0.6890	33.8000	0.0070	0.5031
10E8 WT 7	0.7330	0.0006	0.0030	0.0006	0.1700	0.9840	1.3900	>50.0000	0.0180	0.7314
10E8 WT 8	1.5800	0.0020	0.0170	0.0040	0.9550	2.4000	1.6800	>50.0000	0.0100	1.1400
10E8 WT 9	9.4100	0.0006	0.0220	0.0010	1.4300	1.8100	0.9750	>50.0000	0.0180	1.1783
10E8 WT 10	>50.0000	0.0001	0.0030	0.0004	0.0810	0.5390	0.7890	>50.0000	0.0030	0.3489
10E8 WT 11	>50.0000	0.0020	0.0330	0.0030	2.3100	0.4890	1.1100	>50.0000	0.0840	1.3941
Geometric mean	13.1538	0.0010	0.0074	0.0018	0.6724	0.9669	0.9478	44.6689	0.0142	0.8286
Geometric standard deviation	5.653	2.623	2.692	2.386	2.662	1.757	1.423	1.311	2.382	1.505

1.0 Geometric standard deviation = 1.50 fold; 2.5 Geometric standard deviations = 2.76 fold

<0.001	.001-.01	.01-.100	.100-1.00	1.00-10.0	>10.0

Figure 1. Surface-Matrix Screening to Improve Neutralization Potency of Antibody 10E8

(A) Hypothesis-driven deductive approach (left) versus hypothesis-independent surface-matrix approach (right). The broad sampling of the matrix approach provides extensive information linking surface chemistry to biological functionalities of interest. Shown is the 10E8 Fab with heavy chain in light blue and light chain in white, and with gp41 peptide in magenta.

(B) Schematic flow diagram of surface-matrix approach.

(C) Selection of a 9-virus panel (shown as red in dendrogram) from the 208-isolate panel for neutralization assessment. The clade of each selected strain is displayed in parentheses.

(D) Experimental variation in neutralization. Strains with non-sigmoidal neutralization curves and high assay-replication error are shown in italics.

(E) Minimum observable signal as a function of assay variability and number of variants screened (see Figure S2).

(F) Neutralization IC_{50} by 10E8 variants, arranged by geometric mean IC_{50}-fold improvement for all viruses shown. ">50" was considered as "50" in geometric mean calculations.

(G) Crystal structure of gp41 peptide (magenta) complexed with improved antibody 10E8v4-5R+100cF (light blue, heavy chain; white, light chain).

See also Figures S1 and S2 and Tables S1C and S2.

N-linked glycans were the largest steric substitutions introduced, and deleterious *N*-linked glycan mutations mapped to both of the identified surfaces. We observed strongly deleterious Phe/Trp mutations to cluster to the membrane-facing surface, an unexpected result, as Phe/Trp should enhance membrane interactions. For the 7-glycine mutations, we also observed deleterious mutations to cluster to the membrane-facing surface. The prevalence of the deleterious Phe/Trp and 7-glycine mutations on the expected membrane-facing surface may reflect requirements for specificity in 10E8 interactions with membrane. Arg

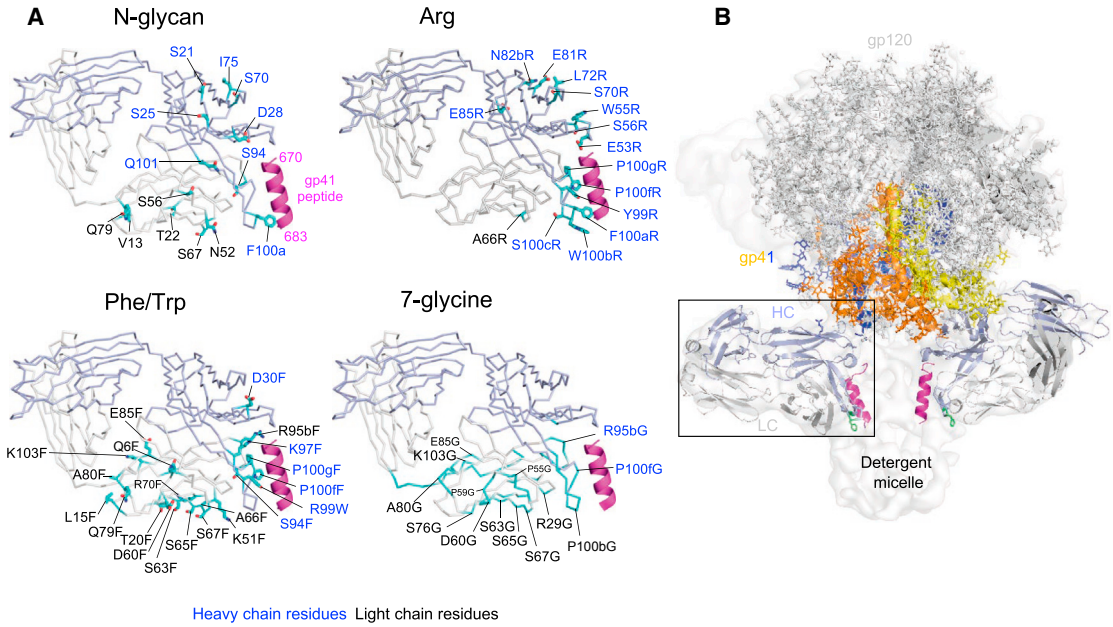

Figure 2. Interactive Surfaces Identified by Surface-Matrix Screening

(A) Crystal structure of Fab 10E8 is shown with residues (cyan) that, when altered by surface-matrix screening, decreased neutralization by over 3 SDs (3.4-fold). Residue alteration types are noted above each structure, with all surface-matrix screening results are shown in Figure S1. Notably, two surfaces, one facing the expected position of the Env trimer and the other facing membrane, are identified by clusters of inhibitory N-glycan mutations. These are not seen in Arg mutations, but the putative membrane-interactive surface is identified by both Phe/Trp and 7-glycine mutations. Note that orientations shown in (A) allow better labeling and are slightly different from 10E8 orientation in (B).

(B) Orientation of 10E8 Fab bound to detergent-solubilized Env trimer from a detergent-solubilized complex with PGT151 (PDB: 5FUU and EMDB: 3312).

See also Figures S1 and S2 and Table S1C.

mutants displayed strong deleterious effects, which mapped mostly to epitope residues. For membrane-facing residues, the lack of deleterious effects (as observed with *N*-glycan, Phe/Trp, and 7-glycine variants) may relate to the ability of Arg to recognize phospholipid head groups. As for Env-facing residues, a few strong negative mutants were observed, which clustered close to a significantly positive mutation, at residue 5.

Chemical Preferences of 10E8 Hotspots Identified in the Surface-Matrix Screen

To provide insight into the chemistry of the $Arg5_{HC}$ and $Phe100c_{HC}$ mutations that improved neutralization potency, we substituted positions 5_{HC} and $100c_{HC}$ in the context of 10E8v4 with other amino acids and assessed their neutralization potency. For $Val5_{HC}$, the positively charged substitutions Lys and Arg were most potent, reducing the median 80% inhibitory concentration (IC_{80}) on a panel of 13 viruses from 4.0 μg/mL to 2.9 and 1.7 μg/mL, respectively (Figure 3A). Modeling this change in the context of the detergent-solubilized Env trimer with antibodies PGT151 and 10E8 (Lee et al., 2016) suggested that positively charged residues at this position interact with negatively charged sialic acid residues in the glycan shield (Figure 3B, left).

For $S100c_{HC}$, the hydrophobic changes Leu, Phe, and Trp were most potent, reducing the median IC_{80} on a panel of 9 viruses from 0.5 μg/mL to 0.09, 0.02, and 0.01 μg/mL, respectively (Figure 3C). Analysis of 10E8 in the detergent-solubilized Env trimer (Lee et al., 2016) indicated that a Phe at position $100c_{HC}$ would face the detergent micelle and, in the context of neutralization, may therefore interact with the viral membrane (Figure 3B, right).

Analogous Membrane-Binding Functional Hotspot in MPER-Directed Antibody 4E10

To further define the interaction of $Phe100c_{HC}$ on antibody 10E8 with the viral membrane, we investigated the analogous membrane-binding functional hotspot on antibody 4E10 (Cardoso et al., 2005), which binds to the same region of the MPER as 10E8. Diverse studies ranging from electron paramagnetic resonance (EPR) analysis (Song et al., 2009; Sun et al., 2008) to mutational and partitioning analyses (Ofek et al., 2010; Rujas et al., 2017), to crystallographic analysis of Fab in complex with phospholipid headgroups (Irimia et al., 2016, 2017) indicate antibodies 10E8 and 4E10 to co-recognize membrane and MPER peptide. In particular, the orientation suggested by the structure of 10E8 with 1,2 dihexanoyl-*sn*-glycerol-3-phospho-(1'-*rac*-glycerol) and scaffolded MPER (Irimia et al., 2017) would position the indole ring of $Trp100c_{HC}$ to extend into the viral lipid membrane (Figure 4A). Examination of the structure of 4E10 with 1,2 dihexanoyl-*sn*-glycerol-3-phosphate and MPER peptide (Irimia et al., 2016) suggested that a Trp substitution in 4E10 at position $100a_{HC}$ would be similarly positioned to interact with the viral lipid membrane (Figure 4B). Indeed, Trp substitutions of different positions at the apex of the third heavy chain complementarity-determining region (CDR H3) of 4E10 showed only

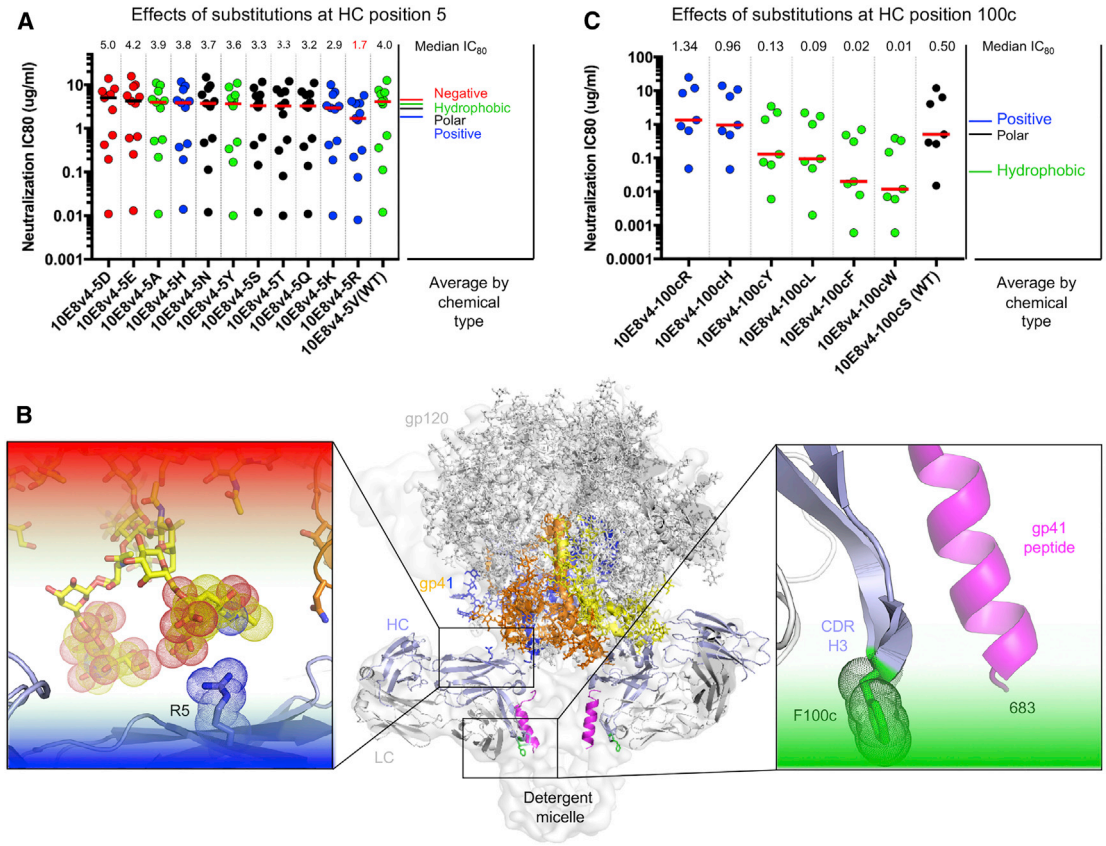

Figure 3. Chemical Preferences of Functional Hotspots Identified by Surface-Matrix Screening

(A) Effects of residue substitutions at heavy chain position 5.

(B) Location of R at position 5 and F at position 100c alteration relative to structure of 10E8 bound to detergent-solubilized Env trimer (insets show residue environments surrounding the two hotspots).

(C) Effects of residue substitutions at heavy chain position 100c.

the substitution at position 100a$_{HC}$ to increase neutralization potency (Figure 4C). Interestingly, superposition of the MPER peptide to provide a common reference frame indicated the CDR H3s of 10E8v4 and 4E10 to interact with different faces of the MPER helix, with the potency-increasing Trp substitutions in each case placed in an analogous position relative to the plane of the viral membrane but not relative to the face of the MPER helix (Figure 4D). Overall, these results show how hydrophobic substitution can enhance the neutralization potency of both antibodies 10E8v4 and 4E10, with substitutions positioned analogously—not relative to the face of the MPER helix but relative to the viral membrane.

To further investigate the Trp-enhanced 10E8v4 and 4E10 interactions with MPER, we used biolayer interferometry (BLI) and surface plasmon resonance (SPR) to measure the interaction between antibody and MPER peptide and between antibody and lipid bilayers containing MPER peptide, respectively. We observed the affinity of 10E8v4 and 10E8v4-100cW to MPER to be virtually identical, as were the affinities of 4E10 and 4E10-100aW (Figure 5A). By contrast, Trp-substituted 10E8v4-100cW and 4E10-100aW appeared to show an increased level of binding to MPER over that of 10E8v4 and 4E10 in the membrane context (Figure 5B). The BLI and SPR measurements thus confirm that the Trp substitutions do not impact MPER affinity but rather impact the co-recognition of MPER and membrane.

Polyreactivity for Membrane-Interacting HIV-1 Broadly Neutralizing Antibodies

In addition to 4E10, a number of other HIV-1 broadly neutralizing antibodies have been proposed to interact with viral membrane, including antibodies 2F5 (Ofek et al., 2004), CAP248-2B (Wibmer et al., 2017), and DH511 (Williams et al., 2017) (Figure 5C). As polyreactivity, such as indicated by binding to HEp2 cells or to cardiolipin, can negatively impact the therapeutic efficacy of these antibodies, we assessed the polyreactivity of six membrane-interacting HIV-1 broadly neutralizing antibodies and of Trp-enhanced functional variants for four of the antibodies (Figure 5D; Figure S3). Notably, all of the Trp-enhanced functional variants tested showed strong polyreactivity, except 10E8v4-100cW.

To understand the reduced polyreactivity of 10E8v4-100cW relative to other Trp-enhanced broadly neutralizing antibodies, we examined the lipophilicity of the proposed membrane-interacting residues in each antibody (Figures 5E and 5F). While the

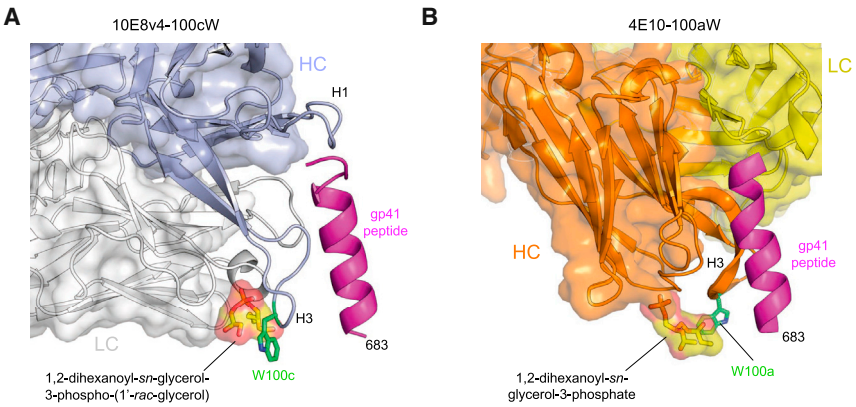

Figure 4. MPER-Directed Antibody 4E10 Shares the Membrane-Binding Functional Hotspot of 10E8

(A) Structural model of antibody 10E8v4 recognizing lipid headgroups, as defined by Irimia et al. (2017), with hotspot position 100c shown in green.

(B) Structural model of antibody 4E10 recognizing lipid headgroups, as defined by Irimia et al. (2016).

(C) Virus neutralization by 4E10 and variants showing 100aW with improved activity.

(D) Superposition gp41 peptide as recognized by 4E10 and 10E8 identifies 4E10 CDR H3 as a hotspot of functional enhancement.

C

IC_{80} (μg/ml)

Clade	Virus	4 E10	4E10-99W	4E10-100aW	4E10-100cW	4E10-100dW
B	YU2.DG.SG3	>50	20.4	3.66	13.9	38.0
B	6101.10.SG3	1.74	1.23	0.232	2.33	2.05
C	ZM106.9.SG3	49.3	20.5	5.35	29.5	38.6
B	PVO.04.SG3	>50	>50	11.2	>50	>50
C	ZM215.8.SG3	4.77	4.40	0.746	3.92	5.91
C	CNE31.SG3	23.9	13.4	1.91	9.19	15.7
ACD	6095.V1.C10.SG3	0.139	0.096	0.012	0.047	0.119
A	KER2008.12.SG3	18.7	11.3	2.37	19.5	12.7
AE	TH966.8.SG3	1.12	1.19	0.130	0.864	1.14
	Median IC_{80}	4.770	7.850	1.910	6.555	9.305
	Geometric Mean	4.327	3.751	0.864	3.585	5.131

Color shading represents potency as .01-.100 .100-1.00 1.00-10.0 10.0-50

D

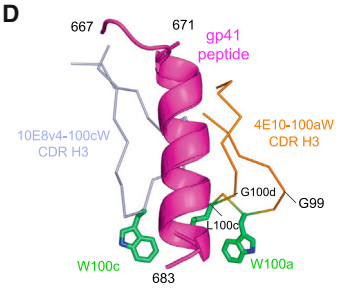

introduction of Trp increased hydrophobicity in each case, 10E8v4-100cW showed the lowest propensity to interact with membrane of all of the Trp-enhanced antibodies. Thus, the reduced polyreactivity of 10E8v4-100cW relative to other Trp-enhanced antibodies appears to stem from an overall lower hydrophobicity of the membrane-interacting component of 10E8.

Glycan-Shield-Interacting Variants of 10E8

In addition to an Arg at position 5_{HC}, a number of other Arg substitutions displayed enhanced neutralization potency, including alterations at positions 7_{HC} and 21_{HC} (Table S1C). Modeling these Arg substitutions in the context of the cryo-EM structure of the detergent-solubilized 10E8-bound Env trimer (Lee et al., 2016) indicated that these Arg substitutions cluster on the heavy chain and potentially interact with sialic acids in the HIV-1 glycan shield (Figure 6A).

We tested these Arg mutations, individually and in combination, for their effects on HIV-1 neutralization as assessed on a panel of nine viruses (Table S1D). Notably, we observed $Val5_{HC}Arg$ to increase neutralization potency in the contexts of 10E8v4, of 10E8v4-100cF, and of 10E8v4-100cW (Figure 6B). Unexpectedly, we also observed several of the Arg substitutions to display substantial polyreactivity (Figures 6B and S4), especially in the context of 100cW, which has heightened polyreactivity of 10E8v4 or 10E8v4-100cF. We note, however, that the mild level of polyreactivity observed for 10E8v4-5R+100cF has been observed with other antibodies, both natural and improved, and that this level of polyreactivity is often tolerated (Rudicell et al., 2014). Interestingly, the largest improvements in neutralization potency came for the introduction of single, not double, Arg residues (Figure 6C). Thus, while Arg substitutions to the Env-facing surface of 10E8 did increase neutralization potency, in some instances, polyreactivity was also increased.

Properties of 10E8v4-5R+100cF

We analyzed, in detail, manufacturing characteristics of three variants, 10E8v4-100cW, 10E8v4-100cF, and 10E8v4-5R+100cF. While 10E8v4-100cW was most potent, it displayed substantial losses during concentration by ultrafiltration, which may be problematic for manufacturing (Figure 7A). While 10E8v4-100cF and 10E8v4-5R+100cF showed acceptable concentration characteristics, 10E8v4-5R+100cF was both more potent and more soluble.

We assessed the half-life in rhesus macaques for each of these three variants, modified by the "LS" half-life-extending mutations (Zalevsky et al., 2010). Notably, all of the variants tracked closely with VRC01-LS through day 14 and appeared to have reduced clearance relative to the parent 10E8 (Figure 7B).

On our 208-isolate panel, 10E8v4-5R+100cF displayed a median IC_{50} of 0.050 μg/mL (Figure 7C; Table S1E), about 2-fold better than that of the recently described N6 antibody, a broadly neutralizing antibody that targets the CD4-binding site (Huang et al., 2016a). The IC_{50}s of 10E8v4-5R+100cF compared favorably with other HIV-1 broadly neutralizing antibodies being prepared for clinical evaluations, with only PGDM1400 showing a more potent median IC_{50} (10E8v4-5R+100cF has substantially higher breadth than PGDM1400). We predicted the extent of complete neutralization (defined as >95% neutralization of a pseudovirus) for each antibody (Experimental Procedures; Table S1F) and found that 10E8v4-5R+100cF completely neutralized 96.6% of the viruses at 10 μg/mL, better than all other antibodies (the next best was N6, with 91.8% viruses completely neutralized).

Since combinations of antibodies can increase breadth and potency over individual antibodies (Kong et al., 2015) and might be needed for efficacy in the prevention of diverse HIV-1 infections (Wagh et al., 2016), we explicitly tested the combination of 10E8v4-5R+100cF with N6 (Figure 7C) and observed this

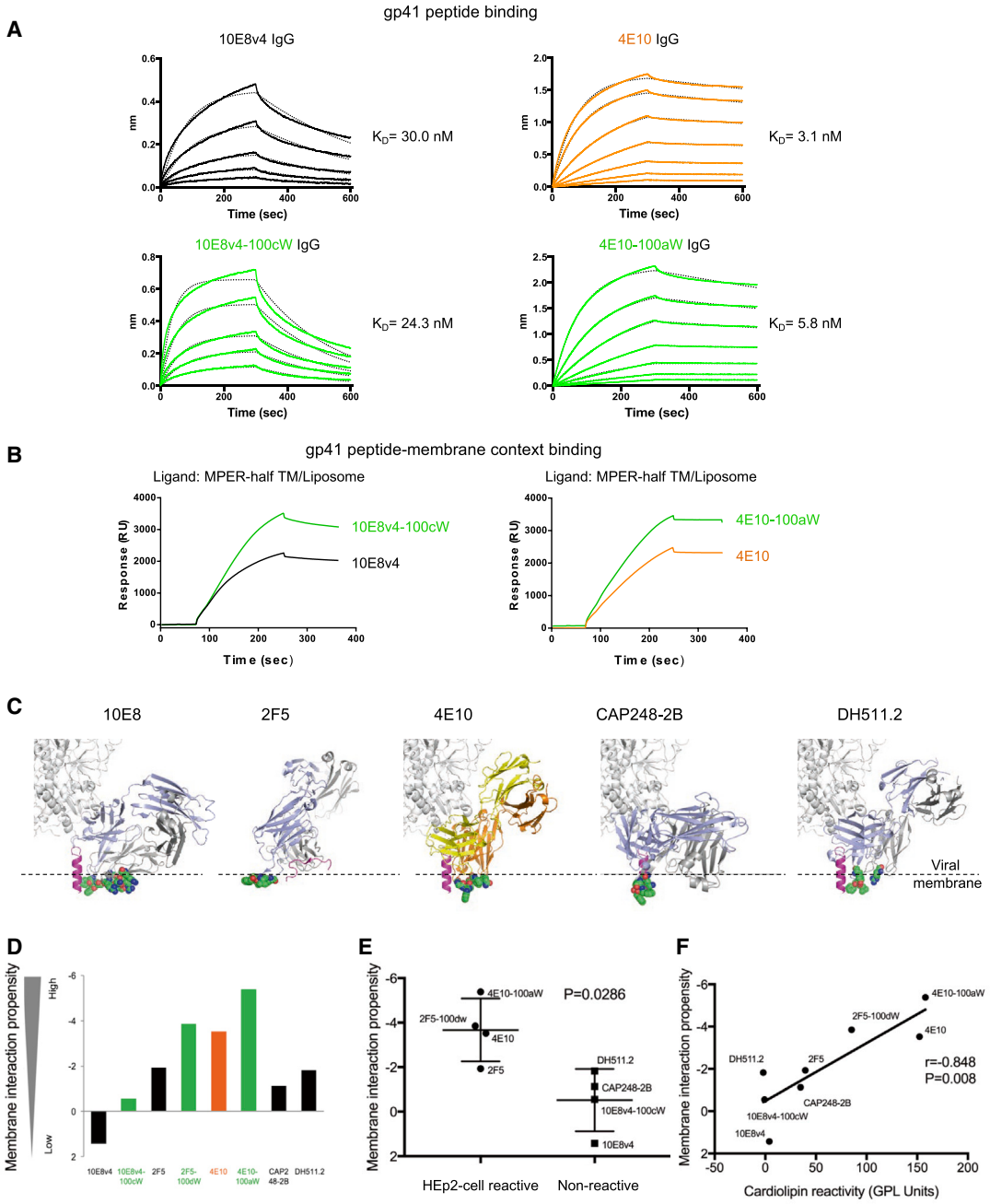

Figure 5. Enhanced Binding to gp41 Peptide in a Membrane Context by 10E8v4-100cW and 4E10-100aW IgGs Modeled Membrane-Epitope Co-recognition and Polyreactivity for Several HIV-1-Neutralizing Antibodies

(A) Binding of 10E8v4, 4E10, 10E8v4-100cW, and 4E10-100aW variants to MPER peptide. IgG, immunoglobulin G. K_D, equilibrium dissociation constant.

(B) Binding of 10E8v4, 4E10, 10E8v4-100cW, and 4E10-100aW variants to lipid bilayers containing MPER peptide.

(C) Membrane proximal residues (shown in spheres) for 10E8, 4E10, CAP248-2B, DH511.2, and 2F5. Positions of viral membrane surface approximated by dashed line (Supplemental Experimental Procedures).

(D) Membrane interaction propensity of membrane-proximal residues.

(E) HEp2 cell binding versus lipophilicity. Error bars represent SD.

(F) Cardiolipin binding versus lipophilicity.

See also Figure S3.

A

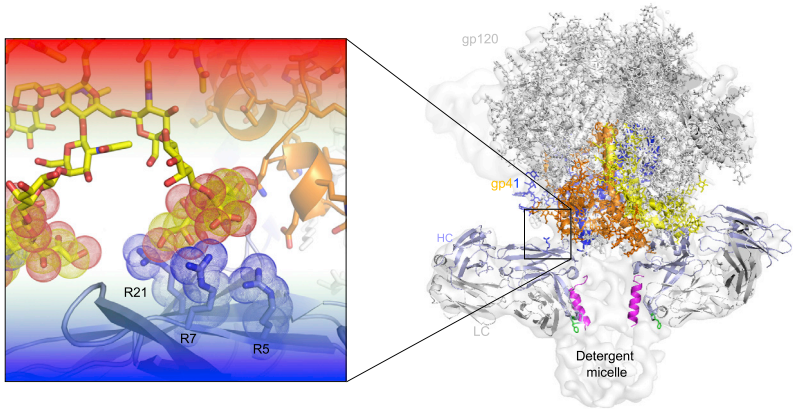

B

Impact of Arg additions on the neutralization and polyreactivity of 10E8 variants

Antibody	Arg addition	Median IC_{50} (μg/ml)	Relative IC_{50} improvement of Arg	HEp2 ANA
10E8v4	none	2.700	0%	Not reactive
10E8v4-V5R	5R	2.090	29%	Not reactive
10E8v4 -V5R+S7R	5R+7R	1.600	69%	Mild reactivity
10E8v4-100cF	none	0.374	0%	Not reactive
10E8v4-V5R+100cF	5R	0.179	109%	Mild reactivity
10E8v4-100cW	None	0.221	0%	Not reactive
10E8v4-V5R+100cW	5R	0.104	112%	Polyreactive
10E8v4-S21R+100cW	21R	0.073	203%	Polyreactive
10E8v4-V5R+S21R+100cW	5R+21R	0.147	50%	Polyreactive

C

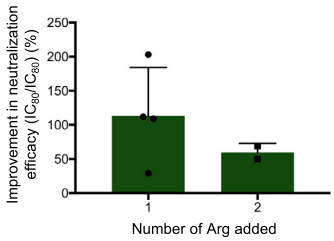

Figure 6. Semi-specific Interactions with Glycan Shield Observed with Hotspot around Heavy Chain Position 5

(A) Modeled glycan shield co-recognition of Arg hits identified by surface-matrix screening of 10E8 variants.

(B) Impact of Arg additions on the neutralization (and polyreactivity) of 10E8 variants.

(C) Average improvement in 10E8 variant neutralization upon the addition of 1 or 2 Arg. Error bars represent SD.

See also Figure S4 and Table S1D.

combination to neutralize all 208 isolates of our cross-clade panel, with an $IC_{50} < 1$ μg/mL of each antibody. We also modeled the performance of the combination of 10E8v4-5R+100cF with other broadly neutralizing antibodies. We used the Bliss-Hill model (Wagh et al., 2016) on individual antibody IC_{50} and IC_{80} data for leading antibody candidates under clinical development against the global 208-virus panel to predict neutralization by all two-antibody combinations of antibodies targeting different epitopes (Experimental Procedures). We compared the performance of two-antibody combinations using not only IC_{80} breadth potency but also completeness of neutralization and simultaneous coverage by both antibodies in the combination (Wagh et al., 2016), and we used target concentrations of 1 μg/mL and 5 μg/mL of each antibody in the combination (Table S1F). We identified the best combination within each epitope class (Table S1F) and compared the best-in-class combinations (Figures 7D and S5). The best overall performance was shown by the combination of 10E8v4-5R+100cF with N6. The main advantages of combining 10E8v4-5R+100cF with N6 were the highest fraction of completely neutralized viruses (96.3%–99.5% viruses, depending on the target concentration as compared to second best of 86.1%–97.6%; p = 0.0002, using Fisher's exact test for 1 μg/mL of each broadly neutralizing antibody) and substantially improved IC_{80} coverage with both antibodies to be active (79.3%–92.8% coverage as compared to second best of 60.6%–69.2%, depending on the target concentration; p values = 6.7×10^{-10} to 4.4×10^{-5}, using Fisher's exact test) (Figure S5). These results suggest that the combination of 10E8v4-5R+100cF with N6 has the potential to neutralize completely a majority of global HIV-1 isolates with both antibodies simultaneously active;thus, passive transfer of this combination could have the potential to prevent majority of infections even at low target concentrations.

DISCUSSION

Improvements in functional efficacy may have substantial impact on antibody therapeutic efficacy. However, standard methods of improvement such as phage display have often floundered, because of differences between antibody-mediated neutralization and antibody-probe binding. Having successfully used surface-screening methods such as arginine scanning to identify sites of antibody interaction (Pancera et al., 2013), we decided to alter the antibody surface and to assess neutralization directly. Importantly, the surface-matrix screening approach does not require determination of the antibody-epitope complex structure. Also, the approach allows for the identification of novel sites of interaction.

While identification of sites of substantial improvement in neutralization potency was our original goal (Figure 1), we observed coherent clustering of strong reductions in neutralization to also impart insight into interactive surfaces (Figure 2). Once functional hotspots for improved neutralization were identified, we could further screen their interactive chemistries (Figure 3). Examination of the $Phe100c_{HC}$ change in the 10E8 context suggested that analogous improvements could be made in the context of the related 4E10 antibody. These changes improved the binding of both 10E8 and 4E10 to MPER in the lipid context (Figures 4 and 5), though issues with polyreactivity prevented full optimization of the semi-specific hydrophobic interactions with

A

Assay	Target values	10E8v4-100cW	10E8v4 -100cF	10E8v4-5R +100cF
Appearance	Clear, colorless; no visible particles	Pre-filtration: visible particles; Post-filtration: clear	Pre-filtration: visible particles; Post-filtration: clear	Pre-filtration: visible particles; Post-filtration: clear
Concentration	Concentration +/- 5% of initial value by A280	~60% loss during concentration	No loss during concentration	No loss during concentration
OD_{350}	$OD_{350} \leq 0.05$	$OD_{350} \leq 0.05$	$OD_{350} \leq 0.05$	$OD_{350} \leq 0.05$
DSC	$T_m1 \geq 65°$ C	T_m1: 69.8° C	T_m1: 72.7° C	T_m1: 70.8° C
CD	Primary minimum at ~218 nm	Min. ~ 217 nm and ~230 nm	Min. ~ 217 nm and ~230 nm	Min. ~ 217 nm and ~230 nm
DLS scans	>95% material in primary population (R_h: ~5-6 nm) Pd ≤ 20%	Pass R_h: 5.8; Pd: 10.0%	Pass R_h: 4.8; Pd: 10.6%	Pass R_h: 5.2; Pd: 13.1%
DLS melt	$T_{onset} \geq 60°C$	T_{onset}= 66.6± 0.1	T_{onset}= 67.7± 0.1	T_{onset}= 66.7± 0.9
Ultrafiltration concentration	Concentration (UF over 6 hours)	*23 mg/mL (60% mass recovery)*	*25 mg/mL (87% mass recovery)*	*42 mg/mL (94% mass recovery)*
Isothermal chemical denaturation	$C_{1/2} \geq 5.5$ at one or more conditions tested	$C_{1/2} \geq 5.5$ (pH ≥ 5 .5 and 0-200 mM NaCl)	$C_{1/2} \geq 5.5$ (pH ≥ 5 .5 and 0-200 mM NaCl)	$C_{1/2} \geq 5.5$ (pH ≥ 5.5 and 0-200 mM NaCl)

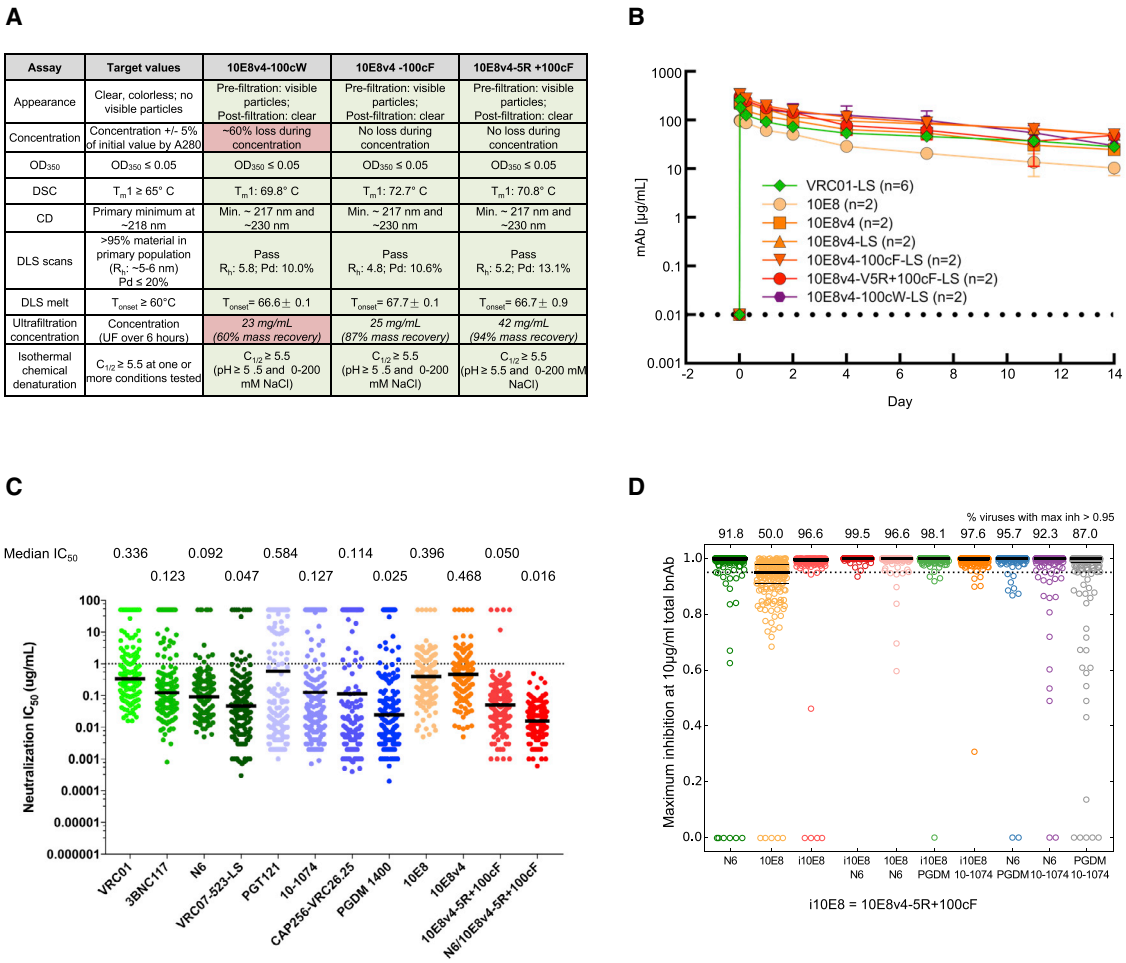

Figure 7. Manufacturing Characteristics, Serum Half-Life, and Neutralization Potency of 10E8 Variants

(A) Manufacturing properties of optimized 10E8 variants. CD, circular dichroism; DLS, dynamic light scattering; DSC, differential scanning calorimetry; OD_{350}, optical density 350; T_m, melting temperature.

(B) Pharmacokinetics of 10E8 variants in rhesus macaque. Error bars represent SD.

(C) Potency of optimized 10E8v4-5R+100cF on a panel of 208 Env pseudoviruses: antibodies shown are being developed for clinical evaluation. Note that the physical combination of N6 with 10E8v4-5R+100cF neutralizes all strains in the 208-isolate panel at less than 1 µg/mL. The median IC_{50} based on all 208 viruses (including all resistant strains) for each antibody is displayed.

(D) Completeness of neutralization by single antibodies (10 µg/mL) and antibody combinations with 5 µg/mL of each antibody (predicted using the Bliss Hill model). The numbers on top indicate the percent viruses that were predicted to be neutralized at >95%.

See also Figure S5 and Tables S1E and S1F.

lipid (Figure 5). Examination of the $Arg5_{HC}$ change, meanwhile, suggested semi-specific electrostatic interactions with sialic acids of the glycan shield; while these could lead to improvements in neutralization potency, considerations of polyreactivity prevented full optimization of these electrostatic interactions (Figure 6). Despite issues of polyreactivity, we nevertheless did achieve significant improvement of 10E8 potency. Overall, optimization of semi-specific interactions provided a means to improve the neutralization potency of antibody 10E8 while maintaining its near pan-neutralization breadth (Figure 7).

We did not observe the neutralization-improving mutations $Arg5_{HC}$ and $Phe100c_{HC}$ in the next-generation sequencing of 10E8 B cell transcripts (Soto et al., 2016), suggesting that the two identified hotspots—one facing Env and the other facing the lipid membrane—may not be fully optimized by *in vivo* methods of affinity maturation, perhaps because of differences between eliciting antigen and the functional target of antibody neutralization. Moreover, we were unable to corroborate with kifunensine-grown virus, a requirement for sialic acid in mediating Arg enhancements of potency, as the kifunensine impacted neutralization from multiple antibodies (e.g., antibody VRC01) that are not known to have sialic acid interactions. Nevertheless, our surface-matrix data, comprising almost 300 individually assessed antibody variants, did provide a comprehensive chemical/functional mapping of the 10E8 surface and corroborated the biological relevance of the cryo-EM structure of the 10E8-bound-JR-FL trimer complex, indicating similarity between 10E8 binding in the detergent-solubilized context of the cryo-EM

structure and the membrane-bound context of the functional spike on infectious virus.

Is there a ceiling to additional improvement? Now that we have identified the mechanistic context of $Arg5_{HC}$ and $Phe100c_{HC}$ improvements, hypothesis-driven means of improvement can be used. Alternatively, it would be fascinating to determine whether a second round of surface-matrix screening could iteratively identify other sites of improvement. It may be helpful in a second round to limit the total number of variants tested, to allow for the identification of changes with only 1.5-fold improvement (Figure S2).

While further improvements are likely possible, the optimized antibody, 10E8v4-5R+100cF, may already have utility in both HIV therapy and prophylaxis, especially in combination with antibody N6. We note that an improved 10E8 antibody has been described that utilized a bi-specific strategy in combination with self-targeting to achieve exquisite potency (Huang et al., 2016b) and that trispecific antibodies engineered with 10E8v4 show substantial protection against simian HIV (SHIV) in rhesus macaques (Huang et al., 2016b; Xu et al., 2017). It will be interesting to see whether the enhancements in neutralization potency—achieved here through optimization of semi-specific interactions—will prove to be a general means to improve antibodies. All broad HIV-1-neutralizing antibodies must accommodate glycan (Stewart-Jones et al., 2016), thereby suggesting that optimization of semi-specific interactions with the glycan shield is likely to allow for improvement of other HIV-1 broadly neutralizing antibodies. Altogether, our results suggest that both surface-matrix screening and optimization of semi-specific interactions provide general strategies for enhancing antibody potency.

EXPERIMENTAL PROCEDURES

In Silico Scanning of Antibody Surface

We performed the following surface matrix screening on 10E8. (1) Phe/Trp scan: for all Fv residues that have a side-chain accessible surface area of greater than 30%, we mutated each Phe/Tyr to Trp and every other non-Cys and non-Trp residue to Phe. (2) Arg scan: for all Fv residues that have a side-chain accessible surface area greater than 30%, we mutated each non-Cys and non-Arg residue to Arg. (3) Glycine scanning: a 7-amino acid window was used to scan through the Fv regions (overlap of 2 amino acids). We mutated each residue in the 7-amino acid window to GLY except for the following: the residue is part of the disulfide bridge, and side-chain accessible surface area is less than 5%. (4) Glycan scanning: for all Fab residues, we applied an in-house computational algorithm, which couples NGlycPred (Chuang et al., 2012) to predict glycan occupancy, to identify suitable positions for introducing N-linked glycosylation sequons. The number of constructs was reduced by clustering based on C_β distances (r = 10 Å). Accessible surface areas were calculated using NACCESS (Hubbard and Thornton, 1993).

Informatics Considerations of Library Size and Assay Reproducibility

Log-normal distribution was used to estimate the distribution of fold improvement when the neutralization of the wild-type antibody was repeated N times. Different N, assay variance (σ_e), and different number of variants that can be characterized in detail were investigated to explore the minimal observable signal. All values were calculated using the R statistical package.

Construct Design, Expression and Purification, and Characterization of Antibody Variants

All variant antibodies were constructed, expressed and purified, and characterized as described in the Supplemental Experimental Procedures.

Virus Isolate Panel Selection

The initial 9-virus panel was compiled based on sequence diversity consideration. The panel was further reduced to five viral strains to rank the surface matrix screening variants by moving strains that gave inconsistent results from the wild-type repeat (KER2008.12) and IC_{50} values that were close to detection limit (6095.V1.C1, TH966.8, and 6101.10).

Neutralization Assays

HIV-1 Env pseudoviruses were prepared by transfecting 293T cells (6×10^6 cells in 50 mL growth medium in a T-175 culture flask) with 10 μg of rev/env expression plasmid and 30 μg of an Env-deficient HIV-1 backbone vector (pSG3ΔEnvelope), using FuGENE 6 Transfection Reagent (Invitrogen). Pseudovirus-containing culture supernatants were harvested 2 days after transfection, filtered (0.45 μm), and stored at −80°C or in the vapor phase of liquid nitrogen. Neutralization was measured using HIV-1 Env pseudoviruses to infect TZM-bl cells, as described previously (Li et al., 2005; Sarzotti-Kelsoe et al., 2014). Briefly, 40 μL of pseudovirus was incubated for 30 min at 37°C with 10 μL of serially diluted test antibody in duplicate wells of a 96-well flat-bottomed culture plate. To keep assay conditions constant, sham medium was used in place of antibody in control wells. The pseudovirus input was set at an MOI of approximately 0.01, which generally results in 100,000 to 400,000 relative light units (RLUs) in a luciferase assay (Bright Glo; Promega, Madison, WI, USA). The same assay was scaled for use in 384-well plates as described previously (Sarzotti-Kelsoe et al., 2014) when testing large numbers of samples; e.g., the panel of 208 viruses. Neutralization curves were fit by nonlinear regression using a 5-parameter hill slope equation, as previously described (Seaman et al., 2010). The IC_{50}s were reported as the antibody concentrations required to inhibit viral entry by 50%.

Prediction of Neutralization by Antibody Combinations

We used previously developed the Bliss-Hill model (Wagh et al., 2016) to predict the IC_{50} and IC_{80} titers, completeness of neutralization, and simultaneous neutralization coverage by both antibodies for two-antibody (Ab) combinations using IC_{50} and IC_{80} data for individual antibodies, as implemented on the web tool CombiNAber at the Los Alamos HIV Database (http://www.hiv.lanl.gov/content/sequence/COMBINABER/combinaber.html). We used the antibodies 3BNC117 and VRC07-523LS (CD4 binding site); CAP256-VRC26.25 and PGDM1400 (V2 glycan); PGT121 and 10-1074 (V3 glycan); and 10E8 and 10E8v4-5R+100cF (MPER), tested against the 208 virus panel, and we analyzed all two-antibody combinations with different epitope targets. We focused on two target concentrations of 1 μg/mL and 5 μg/mL of each antibody and ranked the combinations using geometric mean IC_{80}, percentage of viruses neutralized at >95%, and percentage of viruses with both antibodies active.

Statistical Analyses

The Mann-Whitney U test and Pearson correlation were applied in Figure 5E and Figure 5F, respectively. All tests were performed using GraphPad Prism 7.

DATA AND SOFTWARE AVAILABILITY

The accession number for the atomic coordinate and structure factors for 10E8v4-5R+100cF in complex with HIV-1 gp41 MPER is PDB: 5WDF.

SUPPLEMENTAL INFORMATION

Supplemental Information includes Supplemental Experimental Procedures, five figures, and two tables and can be found with this article online at https://doi.org/10.1016/j.celrep.2018.01.023.

ACKNOWLEDGMENTS

We thank J. Stuckey for assistance with figures and members of the Structural Biology Section and Structural Bioinformatics Core, Vaccine Research Center, for discussions or comments on the manuscript. We thank J. Baalwa, D. Ellenberger, D. Gabuzda, F. Gao, B. Hahn, K. Hong, J. Kim, F. McCutchan,

D. Montefiori, L. Morris, J. Overbaugh, E. Sanders-Buell, G. Shaw, R. Swanstrom, M. Thomson, S. Tovanabutra, C. Williamson, and L. Zhang for HIV-1 envelope plasmids used in our neutralization panel. Support for this work was provided by the Intramural Research Programs of the Vaccine Research Center and the Division of Intramural Research, National Institute of Allergy and Infectious Diseases, NIH, and by grants from the International AIDS Vaccine Initiative's Neutralizing Antibody Consortium and from the Bill and Melinda Gates Foundation. Use of sector 22 (Southeast Region Collaborative Access team) at the Advanced Photon Source was supported by the U.S. Department of Energy, Basic Energy Sciences, Office of Science, under contract number W-31-109-Eng-38.

AUTHOR CONTRIBUTIONS

Conceptualization, Design, & Coordination, Y.D.K., G.-Y.C., B.Z., J.R.M., and P.D.K.; Figure Generation, Manuscript Writing, & Manuscript Revision, Y.D.K., G.-Y.C., B.Z., K.Wagh, B.M.K., L.S., and P.D.K.; Antibody Production, Purification, & Neutralization Assessment, Y.D.K., B.Z., V.J., R.T.B., N.A.D.-R., B.L., M.K.L., K.M., S.O., S.D.S., and J.R.M.; Crystal Structure, Y.D.K.; Antibody Half-Life, A.P., X.C., M.C., K. Wang, J.P.T., and D.G.S.; Polyreactivity Assessment, M.A.; Identification of the S100cW Mutation, T.S.G. and L.S.; Virus Panel Selection, I.S.G.; Arg Screening, M.P.; Glycan Modeling, R.R.; Manufacturing Properties, R.C., L.A.K., and S.D.M.; Antibody-gp41 MPER/Liposome Interactions, M.K. and E.L.R.; Antibody Combination Neutralization Prediction, K. Wagh and B.M.K.; 10E8 Construct, M.C.

DECLARATION OF INTERESTS

The authors declare no competing interests.

Received: July 27, 2017
Revised: November 2, 2017
Accepted: January 8, 2018
Published: February 13, 2018

REFERENCES

Ayyar, B.V., Arora, S., and O'Kennedy, R. (2016). Coming-of-age of antibodies in cancer therapeutics. Trends Pharmacol. Sci. *37*, 1009–1028.

Bar, K.J., Sneller, M.C., Harrison, L.J., Justement, J.S., Overton, E.T., Petrone, M.E., Salantes, D.B., Seamon, C.A., Scheinfeld, B., Kwan, R.W., et al. (2016). Effect of HIV antibody VRC01 on viral rebound after treatment interruption. N. Engl. J. Med. *375*, 2037–2050.

Cardoso, R.M., Zwick, M.B., Stanfield, R.L., Kunert, R., Binley, J.M., Katinger, H., Burton, D.R., and Wilson, I.A. (2005). Broadly neutralizing anti-HIV antibody 4E10 recognizes a helical conformation of a highly conserved fusion-associated motif in gp41. Immunity *22*, 163–173.

Caskey, M., Klein, F., Lorenzi, J.C., Seaman, M.S., West, A.P., Jr., Buckley, N., Kremer, G., Nogueira, L., Braunschweig, M., Scheid, J.F., et al. (2015). Viraemia suppressed in HIV-1-infected humans by broadly neutralizing antibody 3BNC117. Nature *522*, 487–491.

Caskey, M., Schoofs, T., Gruell, H., Settler, A., Karagounis, T., Kreider, E.F., Murrell, B., Pfeifer, N., Nogueira, L., Oliveira, T.Y., et al. (2017). Antibody 10-1074 suppresses viremia in HIV-1-infected individuals. Nat. Med. *23*, 185–191.

Chames, P., Van Regenmortel, M., Weiss, E., and Baty, D. (2009). Therapeutic antibodies: successes, limitations and hopes for the future. Br. J. Pharmacol. *157*, 220–233.

Chuang, G.Y., Boyington, J.C., Joyce, M.G., Zhu, J., Nabel, G.J., Kwong, P.D., and Georgiev, I. (2012). Computational prediction of N-linked glycosylation incorporating structural properties and patterns. Bioinformatics *28*, 2249–2255.

Diskin, R., Scheid, J.F., Marcovecchio, P.M., West, A.P., Jr., Klein, F., Gao, H., Gnanapragasam, P.N., Abadir, A., Seaman, M.S., Nussenzweig, M.C., and Bjorkman, P.J. (2011). Increasing the potency and breadth of an HIV antibody by using structure-based rational design. Science *334*, 1289–1293.

Gorman, J., Soto, C., Yang, M.M., Davenport, T.M., Guttman, M., Bailer, R.T., Chambers, M., Chuang, G.Y., DeKosky, B.J., Doria-Rose, N.A., et al.; NISC Comparative Sequencing Program (2016). Structures of HIV-1 Env V1V2 with broadly neutralizing antibodies reveal commonalities that enable vaccine design. Nat. Struct. Mol. Biol. *23*, 81–90.

Hebert, D.N., Lamriben, L., Powers, E.T., and Kelly, J.W. (2014). The intrinsic and extrinsic effects of N-linked glycans on glycoproteostasis. Nat. Chem. Biol. *10*, 902–910.

Huang, J., Ofek, G., Laub, L., Louder, M.K., Doria-Rose, N.A., Longo, N.S., Imamichi, H., Bailer, R.T., Chakrabarti, B., Sharma, S.K., et al. (2012). Broad and potent neutralization of HIV-1 by a gp41-specific human antibody. Nature *491*, 406–412.

Huang, J., Kang, B.H., Ishida, E., Zhou, T., Griesman, T., Sheng, Z., Wu, F., Doria-Rose, N.A., Zhang, B., McKee, K., et al. (2016a). Identification of a CD4-binding-site antibody to HIV that evolved near-pan neutralization breadth. Immunity *45*, 1108–1121.

Huang, Y., Yu, J., Lanzi, A., Yao, X., Andrews, C.D., Tsai, L., Gajjar, M.R., Sun, M., Seaman, M.S., Padte, N.N., and Ho, D.D. (2016b). Engineered bispecific antibodies with exquisite HIV-1-neutralizing activity. Cell *165*, 1621–1631.

Hubbard, S.J., and Thornton, J.M. (1993). NACCESS computer program (Department of Biochemistry and Molecular Biology, University College London).

Hwang, W.Y., and Foote, J. (2005). Immunogenicity of engineered antibodies. Methods *36*, 3–10.

Irimia, A., Sarkar, A., Stanfield, R.L., and Wilson, I.A. (2016). Crystallographic identification of lipid as an integral component of the epitope of HIV broadly neutralizing antibody 4E10. Immunity *44*, 21–31.

Irimia, A., Serra, A.M., Sarkar, A., Jacak, R., Kalyuzhniy, O., Sok, D., Saye-Francisco, K.L., Schiffner, T., Tingle, R., Kubitz, M., et al. (2017). Lipid interactions and angle of approach to the HIV-1 viral membrane of broadly neutralizing antibody 10E8: Insights for vaccine and therapeutic design. PLoS Pathog. *13*, e1006212.

Klein, F., Halper-Stromberg, A., Horwitz, J.A., Gruell, H., Scheid, J.F., Bournazos, S., Mouquet, H., Spatz, L.A., Diskin, R., Abadir, A., et al. (2012). HIV therapy by a combination of broadly neutralizing antibodies in humanized mice. Nature *492*, 118–122.

Kong, R., Louder, M.K., Wagh, K., Bailer, R.T., deCamp, A., Greene, K., Gao, H., Taft, J.D., Gazumyan, A., Liu, C., et al. (2015). Improving neutralization potency and breadth by combining broadly reactive HIV-1 antibodies targeting major neutralization epitopes. J. Virol. *89*, 2659–2671.

Kwon, Y.D., Georgiev, I.S., Ofek, G., Zhang, B., Asokan, M., Bailer, R.T., Bao, A., Caruso, W., Chen, X., Choe, M., et al. (2016). Optimization of the solubility of HIV-1-neutralizing antibody 10E8 through somatic variation and structure-based design. J. Virol. *90*, 5899–5914.

Lee, J.H., Ozorowski, G., and Ward, A.B. (2016). Cryo-EM structure of a native, fully glycosylated, cleaved HIV-1 envelope trimer. Science *351*, 1043–1048.

Li, M., Gao, F., Mascola, J.R., Stamatatos, L., Polonis, V.R., Koutsoukos, M., Voss, G., Goepfert, P., Gilbert, P., Greene, K.M., et al. (2005). Human immunodeficiency virus type 1 env clones from acute and early subtype B infections for standardized assessments of vaccine-elicited neutralizing antibodies. J. Virol. *79*, 10108–10125.

McLellan, J.S., Pancera, M., Carrico, C., Gorman, J., Julien, J.P., Khayat, R., Louder, R., Pejchal, R., Sastry, M., Dai, K., et al. (2011). Structure of HIV-1 gp120 V1/V2 domain with broadly neutralizing antibody PG9. Nature *480*, 336–343.

Ofek, G., Tang, M., Sambor, A., Katinger, H., Mascola, J.R., Wyatt, R., and Kwong, P.D. (2004). Structure and mechanistic analysis of the anti-human immunodeficiency virus type 1 antibody 2F5 in complex with its gp41 epitope. J. Virol. *78*, 10724–10737.

Ofek, G., McKee, K., Yang, Y., Yang, Z.Y., Skinner, J., Guenaga, F.J., Wyatt, R., Zwick, M.B., Nabel, G.J., Mascola, J.R., and Kwong, P.D. (2010). Relationship between antibody 2F5 neutralization of HIV-1 and hydrophobicity of its

heavy chain third complementarity-determining region. J. Virol. *84*, 2955–2962.

Pancera, M., Zhu, J., O'Dell, S., Yang, Y., Zhang, B., Changela, A., McLellan, J.S., Wu, X., Zhou, T., Burton, D.R., et al. (2013). Arginine-scanning of PG16 paratope defines quaternary epitope. AIDS Res. Hum. Retroviruses *29*, A59–A60.

Ramilo, O., Lagos, R., Sáez-Llorens, X., Suzich, J., Wang, C.K., Jensen, K.M., Harris, B.S., Losonsky, G.A., and Griffin, M.P.; Motavizumab Study Group (2014). Motavizumab treatment of infants hospitalized with respiratory syncytial virus infection does not decrease viral load or severity of illness. Pediatr. Infect. Dis. J. *33*, 703–709.

Robison, A.D., Sun, S., Poyton, M.F., Johnson, G.A., Pellois, J.P., Jungwirth, P., Vazdar, M., and Cremer, P.S. (2016). Polyarginine interacts more strongly and cooperatively than polylysine with phospholipid bilayers. J. Phys. Chem. B *120*, 9287–9296.

Roopenian, D.C., and Akilesh, S. (2007). FcRn: the neonatal Fc receptor comes of age. Nat. Rev. Immunol. *7*, 715–725.

Rudicell, R.S., Kwon, Y.D., Ko, S.Y., Pegu, A., Louder, M.K., Georgiev, I.S., Wu, X., Zhu, J., Boyington, J.C., Chen, X., et al.; NISC Comparative Sequencing Program (2014). Enhanced potency of a broadly neutralizing HIV-1 antibody in vitro improves protection against lentiviral infection in vivo. J. Virol. *88*, 12669–12682.

Rujas, E., Caaveiro, J.M., Insausti, S., García-Porras, M., Tsumoto, K., and Nieva, J.L. (2017). Peripheral membrane interactions boost the engagement by an anti-HIV-1 broadly neutralizing antibody. J. Biol. Chem. *292*, 5571–5583.

Sarzotti-Kelsoe, M., Bailer, R.T., Turk, E., Lin, C.L., Bilska, M., Greene, K.M., Gao, H., Todd, C.A., Ozaki, D.A., Seaman, M.S., et al. (2014). Optimization and validation of the TZM-bl assay for standardized assessments of neutralizing antibodies against HIV-1. J. Immunol. Methods *409*, 131–146.

Scheid, J.F., Mouquet, H., Ueberheide, B., Diskin, R., Klein, F., Oliveira, T.Y., Pietzsch, J., Fenyo, D., Abadir, A., Velinzon, K., et al. (2011). Sequence and structural convergence of broad and potent HIV antibodies that mimic CD4 binding. Science *333*, 1633–1637.

Scheid, J.F., Horwitz, J.A., Bar-On, Y., Kreider, E.F., Lu, C.L., Lorenzi, J.C., Feldmann, A., Braunschweig, M., Nogueira, L., Oliveira, T., et al. (2016). HIV-1 antibody 3BNC117 suppresses viral rebound in humans during treatment interruption. Nature *535*, 556–560.

Schoofs, T., Klein, F., Braunschweig, M., Kreider, E.F., Feldmann, A., Nogueira, L., Oliveira, T., Lorenzi, J.C., Parrish, E.H., Learn, G.H., et al. (2016). HIV-1 therapy with monoclonal antibody 3BNC117 elicits host immune responses against HIV-1. Science *352*, 997–1001.

Seaman, M.S., Janes, H., Hawkins, N., Grandpre, L.E., Devoy, C., Giri, A., Coffey, R.T., Harris, L., Wood, B., Daniels, M.G., et al. (2010). Tiered categorization of a diverse panel of HIV-1 Env pseudoviruses for assessment of neutralizing antibodies. J. Virol. *84*, 1439–1452.

Song, L., Sun, Z.Y., Coleman, K.E., Zwick, M.B., Gach, J.S., Wang, J.H., Reinherz, E.L., Wagner, G., and Kim, M. (2009). Broadly neutralizing anti-HIV-1 antibodies disrupt a hinge-related function of gp41 at the membrane interface. Proc. Natl. Acad. Sci. USA *106*, 9057–9062.

Song, R., Oren, D.A., Franco, D., Seaman, M.S., and Ho, D.D. (2013). Strategic addition of an N-linked glycan to a monoclonal antibody improves its HIV-1-neutralizing activity. Nat. Biotechnol. *31*, 1047–1052.

Soto, C., Ofek, G., Joyce, M.G., Zhang, B., McKee, K., Longo, N.S., Yang, Y., Huang, J., Parks, R., Eudailey, J., et al.; NISC Comparative Sequencing Program (2016). Developmental pathway of the MPER-directed HIV-1-neutralizing antibody 10E8. PLoS ONE *11*, e0157409.

Stewart-Jones, G.B., Soto, C., Lemmin, T., Chuang, G.Y., Druz, A., Kong, R., Thomas, P.V., Wagh, K., Zhou, T., Behrens, A.J., et al. (2016). Trimeric HIV-1-Env structures define glycan shields from clades A, B, and G. Cell *165*, 813–826.

Sun, Z.Y., Oh, K.J., Kim, M., Yu, J., Brusic, V., Song, L., Qiao, Z., Wang, J.H., Wagner, G., and Reinherz, E.L. (2008). HIV-1 broadly neutralizing antibody extracts its epitope from a kinked gp41 ectodomain region on the viral membrane. Immunity *28*, 52–63.

Trevino, S.R., Scholtz, J.M., and Pace, C.N. (2007). Amino acid contribution to protein solubility: Asp, Glu, and Ser contribute more favorably than the other hydrophilic amino acids in RNase Sa. J. Mol. Biol. *366*, 449–460.

Wagh, K., Bhattacharya, T., Williamson, C., Robles, A., Bayne, M., Garrity, J., Rist, M., Rademeyer, C., Yoon, H., Lapedes, A., et al. (2016). Optimal combinations of broadly neutralizing antibodies for prevention and treatment of HIV-1 clade C infection. PLoS Pathog. *12*, e1005520.

Wibmer, C.K., Gorman, J., Ozorowski, G., Bhiman, J.N., Sheward, D.J., Elliott, D.H., Rouelle, J., Smira, A., Joyce, M.G., Ndabambi, N., et al. (2017). Structure and recognition of a novel HIV-1 gp120-gp41 interface antibody that caused MPER exposure through viral escape. PLoS Pathog. *13*, e1006074.

Williams, L.T.D., Ofek, G., Schatzle, S., McDaniel, J.R., Lu, X., Nicely, N.I., Wu, L., Lougheed, C., Bradley, T., Louder, M., et al. (2017). Potent and broad HIV-neutralizing antibodies in memory B cells and plasma. Sci. Immunol. *2*, eaal2200.

Wu, H., Pfarr, D.S., Johnson, S., Brewah, Y.A., Woods, R.M., Patel, N.K., White, W.I., Young, J.F., and Kiener, P.A. (2007). Development of motavizumab, an ultra-potent antibody for the prevention of respiratory syncytial virus infection in the upper and lower respiratory tract. J. Mol. Biol. *368*, 652–665.

Wu, X., Yang, Z.Y., Li, Y., Hogerkorp, C.M., Schief, W.R., Seaman, M.S., Zhou, T., Schmidt, S.D., Wu, L., Xu, L., et al. (2010). Rational design of envelope identifies broadly neutralizing human monoclonal antibodies to HIV-1. Science *329*, 856–861.

Xu, L., Pegu, A., Rao, E., Doria-Rose, N., Beninga, J., McKee, K., Lord, D.M., Wei, R.R., Deng, G., Louder, M., et al. (2017). Trispecific broadly neutralizing HIV antibodies mediate potent SHIV protection in macaques. Science *358*, 85–90.

Young, L., Jernigan, R.L., and Covell, D.G. (1994). A role for surface hydrophobicity in protein-protein recognition. Protein Sci. *3*, 717–729.

Zalevsky, J., Chamberlain, A.K., Horton, H.M., Karki, S., Leung, I.W., Sproule, T.J., Lazar, G.A., Roopenian, D.C., and Desjarlais, J.R. (2010). Enhanced antibody half-life improves in vivo activity. Nat. Biotechnol. *28*, 157–159.

Zhou, T., Zhu, J., Wu, X., Moquin, S., Zhang, B., Acharya, P., Georgiev, I.S., Altae-Tran, H.R., Chuang, G.Y., Joyce, M.G., et al.; NISC Comparative Sequencing Program (2013). Multidonor analysis reveals structural elements, genetic determinants, and maturation pathway for HIV-1 neutralization by VRC01-class antibodies. Immunity *39*, 245–258.

Cell Reports, Volume *22*

Supplemental Information

Surface-Matrix Screening Identifies Semi-specific Interactions that Improve Potency of a Near Pan-reactive HIV-1-Neutralizing Antibody

Young D. Kwon, Gwo-Yu Chuang, Baoshan Zhang, Robert T. Bailer, Nicole A. Doria-Rose, Tatyana S. Gindin, Bob Lin, Mark K. Louder, Krisha McKee, Sijy O'Dell, Amarendra Pegu, Stephen D. Schmidt, Mangaiarkarasi Asokan, Xuejun Chen, Misook Choe, Ivelin S. Georgiev, Vivian Jin, Marie Pancera, Reda Rawi, Keyun Wang, Rajoshi Chaudhuri, Lisa A. Kueltzo, Slobodanka D. Manceva, John-Paul Todd, Diana G. Scorpio, Mikyung Kim, Ellis L. Reinherz, Kshitij Wagh, Bette M. Korber, Mark Connors, Lawrence Shapiro, John R. Mascola, and Peter D. Kwong

SUPPLEMENTAL INFORMATION

Supplemental Experimental Procedures

Constructs, expression and purification of antibody variants. 298 expression constructs for 10E8 antibody variants were generated with site-directed mutagenesis using 10E8 light or heavy chain expressing pVRC8400 vector as a template. To express variant antibodies, 0.15 ml of Turbo293 transfection reagent (Speed BioSystems) were added to 2.5 ml Opti-MEM medium (Life Technology) and incubated for 5 min at room temperature (RT). Meanwhile, 50 μg of plasmid DNAs (25 μg of heavy chain and 25 μg of light chain) were added to 2.5 ml of Opti-MEM medium in another tube. The 2.5 ml Opti-MEM medium containing 0.15 ml of Turbo293 were then mixed with the 2.5 ml Opti-MEM medium containing 50 μg of plasmid DNAs, incubated for 15 min at RT, and added to 40 ml of Expi293 cells (Life Technology) at 2.5 million cells/ml. The transfected cells were cultured in shaker incubator at 120 rpm, 37 °C, 9% CO_2 overnight. On the second day of transfection, 4 ml of AbBooster medium (ABI scientific) were added to each flask of transfected cells and the flasks were transferred to shaker incubators at 120 rpm, 33 °C, 9% CO_2 for additional 5 days. At 6 days after transfection, supernatants were harvested and purified over 0.5 ml Protein A (GE Health Science) resin in columns. Each antibody was eluted with IgG elution buffer (Pierce), immediately neutralized with one tenth volume of 1M Tris-HCL pH 8.0. The antibodies were then buffer exchanged in PBS by dialysis, adjusted concentration to 0.5 mg/ml and filtered (0.22 μm) for neutralization assays.

Crystallization, structure determination and refinement. 10E8v4-5R+100cF IgG was produced and its antigen-binding fragment (Fab) was generated as described (Kwon et al., 2016). For crystallization, 10E8v4-5R+100cF Fab and gp41 peptide ($_{668}$SLWNWFDITKWLWYIK$_{683}$RRR) were mixed 1:3 molar ratio of protein:gp41 peptide and concentrated to ~10 mg/ml in buffer containing 5 mM HEPES, 7.4, 150 mM NaCl. Then the concentrated protein-gp41 peptide complex was robotically screened for crystallization conditions using Hampton Research, Wizard Screen, and Precipitation Synergy Screen. Initial crystallization conditions were further optimized to grow diffracting quality crystals in hanging drop vapor diffusion where the mixture of 0.5 ul of protein and 0.5 ul of reservoir solution was equilibrated against the reservoir solution containing 12% PEG 3350, 5% iso-propanol, and 0.1M Ammonium Citrate, 7.5. Crystals were cryo-protected by soaking into a solution containing 15% glycerol, 15% ethylene glycol, 7.5% 2r3r-butanediol, 12% PEG 3350, 5% iso-propanol, 0.1M Ammonium Citrate, 7.5 and flash frozen in liquid nitrogen for data collection at synchrotron beamline, SER-CAT ID22, Advanced Photon

Source, Argonne National Laboratory. Diffraction data were processed and scaled using HKL2000 (Otwinowski and Minor, 1997). The structure was solved by molecular replacement using search model, PDB ID 5IQ9, with Phaser (McCoy et al., 2007), built with Coot (Emsley and Cowtan, 2004) and refined with PHENIX (Adams et al., 2010). Crystallographic data and refinement statistics are summarized in table S2.

Binding kinetics by bio-layer interferometry. We used Octet RED 384 (*forté*BIO) to determine the binding kinetics of gp41 MPER peptide-antibody interactions. Streptavidin biosensors were wetted in PBS with 1% BSA for 10 min. Then the biosensors were loaded with biotinylated gp41 peptide (biotin-$_{661}$GELDKWASLWNWFNITNWLWYIK$_{683}$) by immersing into 125 nM of the MPER peptide in PBS with 1% BSA for 5 min. IgGs were prepared in 2-fold dilution series in PBS with 1% BSA starting at 250 nM. Association and dissociation were monitored for 5 min. each. The curves were fitted globally by 1:1 binding model to extract the binding kinetics.

Surface plasmon resonance analysis. BIAcore experiments were carried out using a BIAcore 3000 with the Pioneer L1 sensor chip at 25 °C. The running buffer was 20 mM HEPES containing 0.15 M NaCl, pH 7.4. To measure the relative binding reactivity of bnAbs for MPER embedded in membrane, 40 µl of MPER-halfTM/liposome, consisting of MPER-halfTM (HxB2 sequence a.a 662-693) at a 1:50 molar ratio of peptide to lipids using DOPC and DOPG (4:1) with a liposome concentration of 2 mg/ml, was applied to the L1 chip surface at a flow rate of 5 µl/min. To remove any multi-lamellar structures from the lipid surface, sodium hydroxide (20 µl, 25 mM) was injected at a flow rate of 100 µl/min, which resulted in a stable base line corresponding to the immobilized liposome bilayer membrane with response units of 4500-5000. Antibody solution (10 µg/ml) was then passed over the MPER-halfTM/liposome surface for 3 min at a flow rate of 10µl/min. The immobilized liposomes were completely removed with an injection of 40 mM CHAPS (25 µl) at a flow rate of 5µl/min, followed by a 15 µl injection of NaOH (50 mM)/isopropyl alcohol (6:4) at a 50 µl/min flow rate. Each antibody injection was performed on a freshly prepared liposome surface.

Identification of membrane proximal residues. PDB:5FUU (Lee et al., 2016) with fitted MPER/10E8 was reoriented such that the symmetry axis of the JR-FL EnvdCT trimer is along the z-axis. 10E8v4, 4E10, and DH511.2

were aligned onto the model using their corresponding structures in complex with the MPER. CAP248-2B was aligned onto the model based on aligning a published CAP248-2B/trimer EM model (Wibmer et al., 2017). For these four antibodies, residues with at least one heavy atom within five angstroms along the z axis from the C alpha atom of residue 684 were considered as membrane proximal residues. The membrane proximal residues for 2F5 were inferred from prior study of Ofek et al. (Ofek et al., 2004).

Polyreactivity characterization. Antibodies were assessed for auto-reactivity on two platforms: anti-nuclear antibodies by staining on HEp2 cells (ZEUS Scientific Cat. No: FA2400, ANA HEp2 Test System) and anti-cardiolipin ELISA (Inova Diagnostics Cat. No: 708625, QUANTA LITE ACA IgG III) as per the manufacturer's instructions. On HEp2 cells, antibodies were tested at 50 and 25 µg/ml. Control antibodies VRC01-LS, 4E10 and VRC07-G54W were included in each slide and assigned a score between 0 and 3+. Test antibodies scored greater than 1+ at 25 µg/ml were considered autoreactive. In the cardiolipin binding assay, monoclonal antibodies scored greater than three times background at 33 µg/ml were considered autoreactive.

Manufacturing characteristics of 10E8 variants

Appearance evaluation. Test samples were visually inspected to assess the color and clarity by examining against both black and white background under fluorescent lighting using a Bosch MIH-DX Manual Visual Inspection Hood. Each vial was gently swirled prior to examination to re-suspend settled particles. Appearance parameters evaluated included color, turbidity, opalescence, visible particle size and frequency.

Concentration determination by UV-Visible spectroscopy. UV-visible spectra were acquired using a single-beam diode array spectrophotometer (Agilent 8453, GE Healthcare) in a 10 mm path length quartz cuvette with a 180 µl useable sample volume. The instrument was blanked with the appropriate buffers and sample data was collected from 200 – 600 nm, with 1 nm data intervals and 0.5 second integration. Optical density was quantified using the signal at 350 nm. Reported absorbance results were light scattering corrected using ChemStation software, calculated in a non-absorbing range (350-500 nm).

Dynamic light scattering. Hydrodynamic radii (Rh) and population size distributions (%Pd) were measured by dynamic light scattering (DLS) using the Wyatt DynaPro Plate Reader and Plate Reader II. Samples were analyzed in a Corning™ 384-well plate (30 µl/well, in two 15 µl aliquots for increased accuracy). Six (6) wells were analyzed per sample (three wells per replicate). Data were acquired at 25 ± 2°C for 10 readings per well, at 10 second per acquisition, reporting particles with an Rh in the range of 2 – 2000 nm. Data were fitted to a correlation function algorithm and the regularization fit hydrodynamic radius and population distribution data were generated using the Dynamics software (Wyatt, version 7.1.7).

Thermal transitions by dynamic light scattering. Thermal ramp dynamic light scattering was performed using the Wyatt DynaPro Plate Reader and Wyatt DynaPro Plate Reader II. Thermal transitions analyses were conducted using a centroid plate arrangement; samples were arrayed (n = 2 per replicate) in a solid rectangle in the center of the plate (30 µl/well, in two 15 µl aliquots for increased accuracy). Additionally, the wells surrounding the samples were filled with high-purity paraffin oil to minimize edge effects and an additional 10 µl of paraffin oil was gently layered on top of the sample-containing wells to minimize evaporation. Data were acquired for 5 readings per well, at 5 seconds per acquisition while the temperature was ramped from 25°C to 70°C at a rate of 0.12°C / minute. Particle data was reported for Rh values in the range of 2 – 5000 nm.

The thermal transition onset (Tonset) for each sample was determined using the onset function (50 – 60°C range with no zero-slope parameter applied) in Dynamics version 7.1.9. Outlying data points and data points for which gross aggregation had occurred (Rh > ~500 nm) were marked until the line of fit overlaid suitably with the remaining data points, as viewed from a y-axis (cumulative Rh) scale of 0 – 150 nm. As transient fluctuations in signal due to aggregation are indistinguishable from contaminant (dust) particle interference, no further data screen was applied.

Differential scanning calorimetry. Differential scanning calorimetry (DSC) analysis was performed using a GE Healthcare VP-Capillary differential scanning calorimeter (DSC). Samples were heated from 10 – 90°C at a rate of 1°C/minute (no reverse scans were acquired). Data were analyzed using MicroCal Origin (version 7.0) and were subjected to buffer subtraction and baseline correction prior to determination of thermal transition midpoints (Tm).

Circular dichroism. Far UV circular dichroism spectroscopy was performed using a Chirascan-plus Circular Dichroism Spectrometer (Applied Photophysics Ltd) equipped with a Peltier temperature controller and a 6-position cuvette holder. Spectra were collected from 195-260 nm for initial scans using a 0.1 cm path length cuvette. Baseline measurement of the buffer was taken and subtracted from sample measurements prior to data analysis.

Isothermal chemical denaturation. Isothermal chemical denaturation experiments were carried out using ICD 2304 Isothermal Chemical Denaturation System (Unchained Labs) equipped with a fluorescence detector. The stability of the monoclonal antibodies in a pH range of 4.5 - 7.0 and NaCl concentration range of 0 - 200 mM was determined by denaturing the samples in a linear gradient of urea from 0 to 9 M. A buffer system of 10 mM sodium phosphate, sodium succinate, and histidine was used to generate the pH range. All dilutions for the pH range, NaCl and urea concentration was performed by the instrument. The denaturation of the antibodies was detected by monitoring the intrinsic fluorescence using an excitation wavelength of 280 nm and recording the emission spectra between 300 - 500 nm. Data processing was performed with the software provided by the instrument to identify the denaturation midpoint (C1/2).

Ultrafiltration. Ultrafiltration was performed using an Amicon Stirred cell concentrator Model:8003 (EMD Millipore) using a 30 kD Ultracel regenerated cellulose filter discs to increase the concentration of the antibodies. Nitrogen gas pressure of ~ 60 psi was applied and the protein solution was stirred constantly to prevent the formation of a concentration gradient. The concentration of the antibody in the cell was monitored over approximately 6 hours by UV-visible spectroscopy as described above.

Antibody half-life in rhesus macaque. Male *Macaca mulatta* animals of Indian origin were used in these studies. All animal experiments were reviewed and approved by the Animal Care and Use Committee of the Vaccine Research Center, NIAID, NIH, and all animals were housed and cared for in accordance with local, state, federal, and institute policies in an American Association for Accreditation of Laboratory Animal Care (AAALAC)-accredited facility at the NIH. Indian rhesus macaques were infused intravenously with 10 mg/kg of monoclonal antibody. Endotoxin levels were measured for each antibody preparation by the QCL-1000™ endpoint chromogenic LAL assay (Lonza) and were all below 0.5 EU/mg levels. Whole blood samples were collected prior to

injection, and at time points 0, 30 mins, 6 hours, 12 hours, and days 1, 2, 4, 7, and 14. Plasma was separated by centrifugation. Plasma samples were heat-inactivated at 56°C for 30 minutes, and lipoproteins were pelleted. Plasma antibody levels were determined by ELISA.

SUPPLEMENTAL REFERENCES

Adams, P.D., Afonine, P.V., Bunkoczi, G., Chen, V.B., Davis, I.W., Echols, N., Headd, J.J., Hung, L.W., Kapral, G.J., Grosse-Kunstleve, R.W., *et al.* (2010). PHENIX: a comprehensive Python-based system for macromolecular structure solution. Acta Crystallogr D Biol Crystallogr *66*, 213-221.

Emsley, P., and Cowtan, K. (2004). Coot: model-building tools for molecular graphics. Acta Crystallogr D Biol Crystallogr *60*, 2126-2132.

Kwon, Y.D., Georgiev, I.S., Ofek, G., Zhang, B., Asokan, M., Bailer, R.T., Bao, A., Caruso, W., Chen, X., Choe, M., *et al.* (2016). Optimization of the Solubility of HIV-1-Neutralizing Antibody 10E8 through Somatic Variation and Structure-Based Design. J Virol *90*, 5899-5914.

Lee, J.H., Ozorowski, G., and Ward, A.B. (2016). Cryo-EM structure of a native, fully glycosylated, cleaved HIV-1 envelope trimer. Science *351*, 1043-1048.

McCoy, A.J., Grosse-Kunstleve, R.W., Adams, P.D., Winn, M.D., Storoni, L.C., and Read, R.J. (2007). Phaser crystallographic software. J Appl Crystallogr *40*, 658-674.

Ofek, G., Tang, M., Sambor, A., Katinger, H., Mascola, J.R., Wyatt, R., and Kwong, P.D. (2004). Structure and mechanistic analysis of the anti-human immunodeficiency virus type 1 antibody 2F5 in complex with its gp41 epitope. J Virol *78*, 10724-10737.

Otwinowski, Z., and Minor, W. (1997). Processing of X-ray diffraction data collected in oscillation mode. Methods Enzymol *276*, 307-326.

Wibmer, C.K., Gorman, J., Ozorowski, G., Bhiman, J.N., Sheward, D.J., Elliott, D.H., Rouelle, J., Smira, A., Joyce, M.G., Ndabambi, N., *et al.* (2017). Structure and Recognition of a Novel HIV-1 gp120-gp41 Interface Antibody that Caused MPER Exposure through Viral Escape. PLoS Pathog *13*, e1006074.

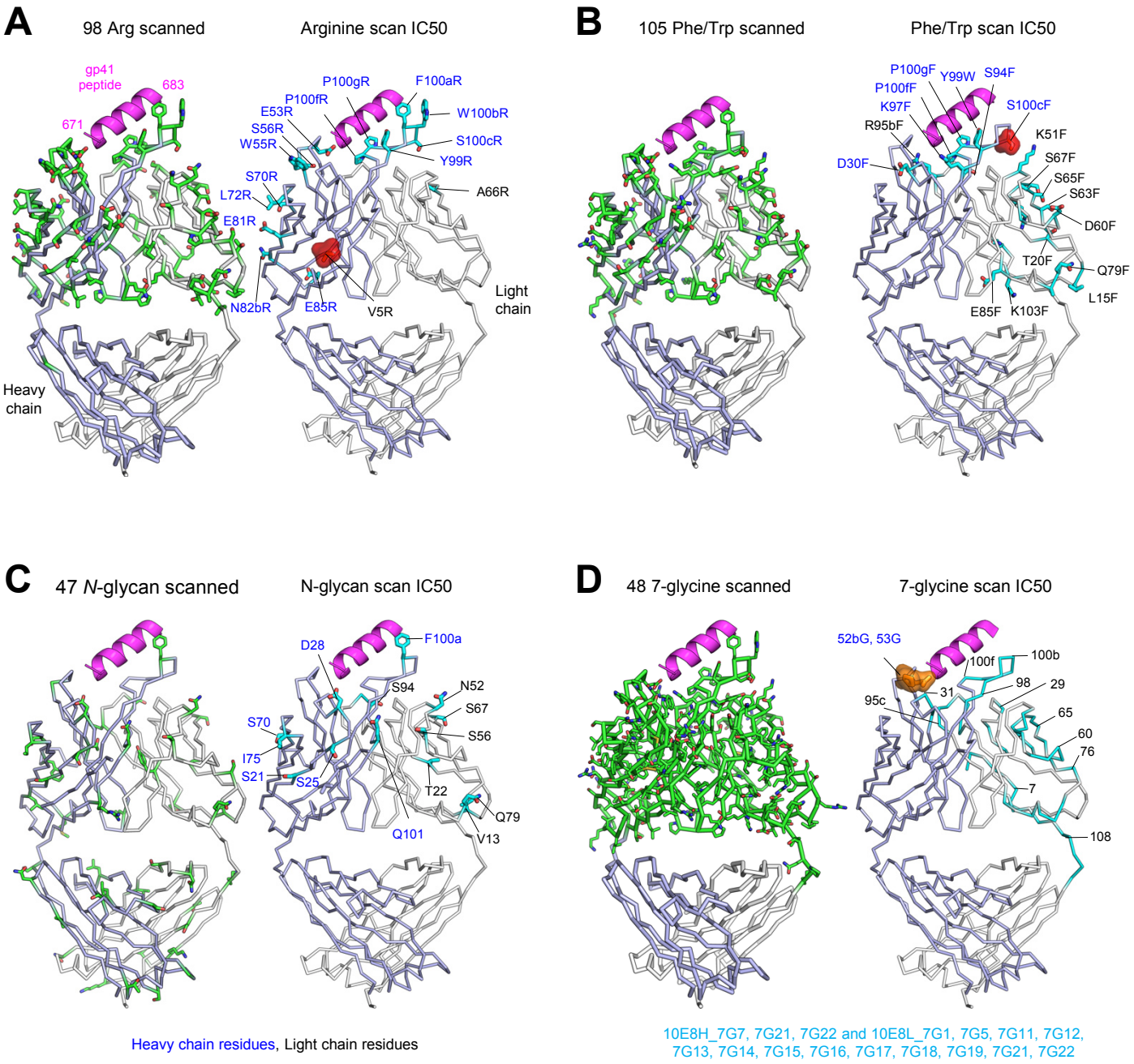

Figure S1. Surface matrix-screening of antibody 10E8 with neutralization readout. Related to Figures 1 and 2. (**A**) 98 10E8 heavy chain (light blue) and light chain (white) residues screened with Arginine for improved potency were shown in stick representation (left) and colored as defined in figure key. (**B**) 105 10E8 heavy and light chain residues screened with Phe/Trp for improved potency were shown in stick representation (left). Phe/Trp variants were shown in the same color scheme as in (A) (right). (**C**) 47 10E8 heavy and light chain residues that were mutated to add an N-linked glycan were shown in stick representation (left). N-linked glycan variants were shown in the same color scheme as in (A) (right). (**D**) 10E8 heavy and light chain residues that were part of 48 7-glycine substituted variants were shown in stick representation (left). Positions which are part of 7-glycine substituted variants were highlighted as in (A) (right). 7-glycine substituted variants with the potency impaired greater than 3.41-fold were listed. See the sequences of the variants in Table S1.

A

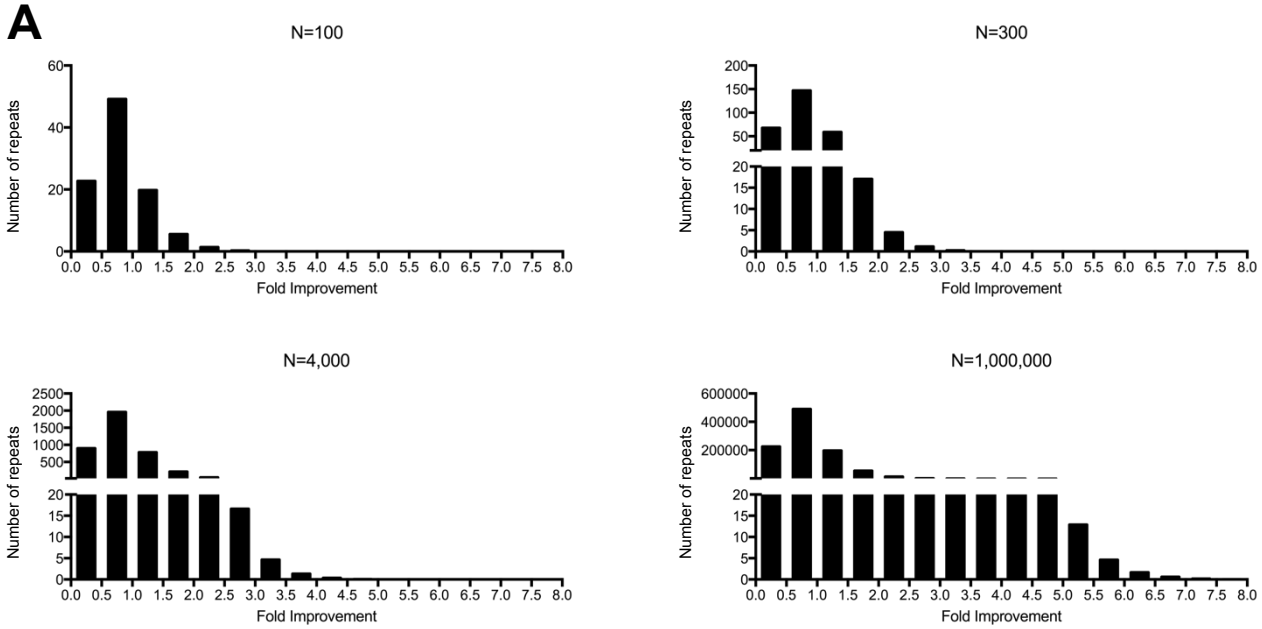

B

	N=100	N=300	N=4000	N=1000000
Fold improvement for top 10	2.84	3.29	4.41	7.27
	2.41	2.84	3.92	6.64
	2.21	2.64	3.7	6.37
	2.08	2.51	3.56	6.18
	1.99	2.41	3.45	6.05
	1.91	2.33	3.37	5.95
	1.85	2.27	3.3	5.86
	1.79	2.21	3.24	5.78
	1.74	2.17	3.19	5.72
	1.7	2.12	3.14	5.66

Figure S2. Minimum observable signal, as a function number of variants screened with an assay variability σ_g of 1.5. Related to Figures 1 and 2. (**A**) Theoretical distribution of fold improvement observed when the same measurement is repeated N times, assuming a log-normal distribution. (**B**) Top ten fold improvement observed when the same measurement is repeated N times.

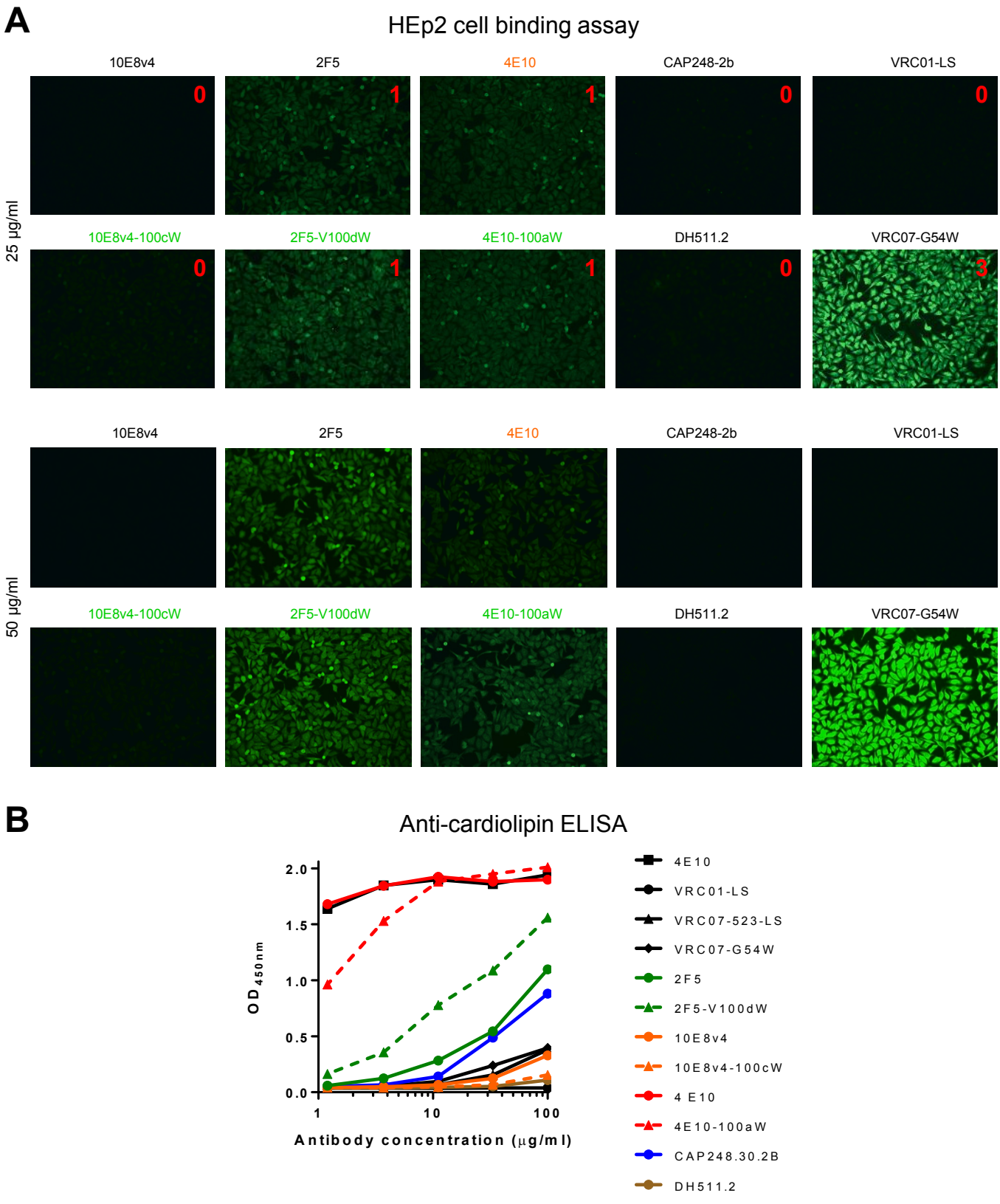

Figure S3. Polyreactivity of 10E8 antibody variants and other MPER-directed antibodies with hydrophobic substitutions. Related to Figure 5. (**A**) In the HEp2 cell staining assay, antibodies were tested at 25 and 50 µg/ml with control antibodies, VRC01-LS, 4E10 and VRC07-G54W. Control antibodies were assigned a score between 0 and 3+. Test antibodies scored greater than 1+ at 25 µg/ml were considered autoreactive. (**B**) Cardiolipin binding assay. Antibodies scored three times greater than background at 33 µg/ml were considered autoreactive.

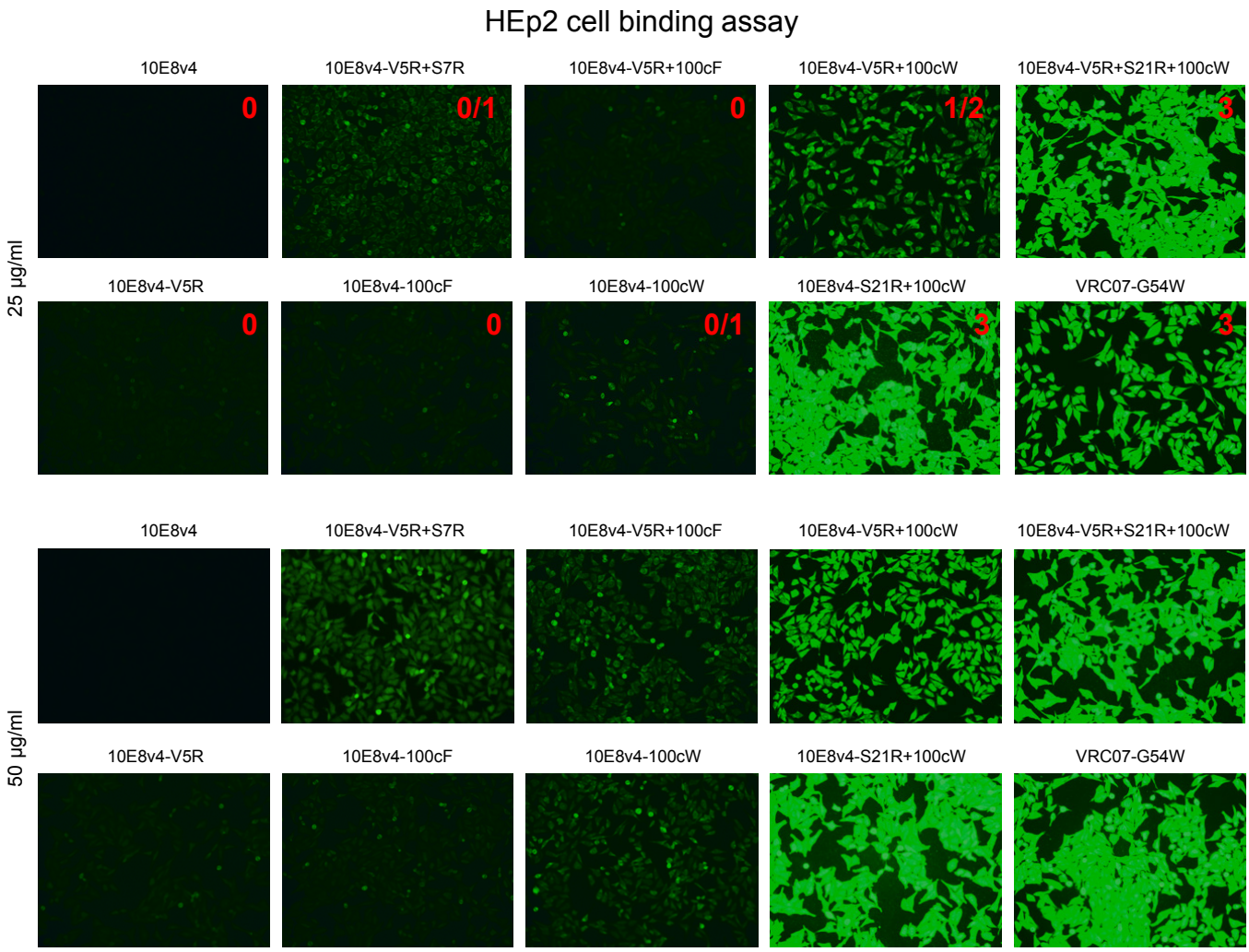

Figure S4. Polyreactivity of 10E8 antibody variants with positively charged substitutions. Related to Figure 6. With HEp2 cell staining assay, antibodies were tested at 25 and 50 µg/ml along with control antibodies, VRC01-LS, 4E10 (shown in Figure S3) and VRC07-G54W. Control antibodies were assigned a score between 0 and 3+. Test antibodies scored greater than 1+ at 25 µg/ml were considered autoreactive.

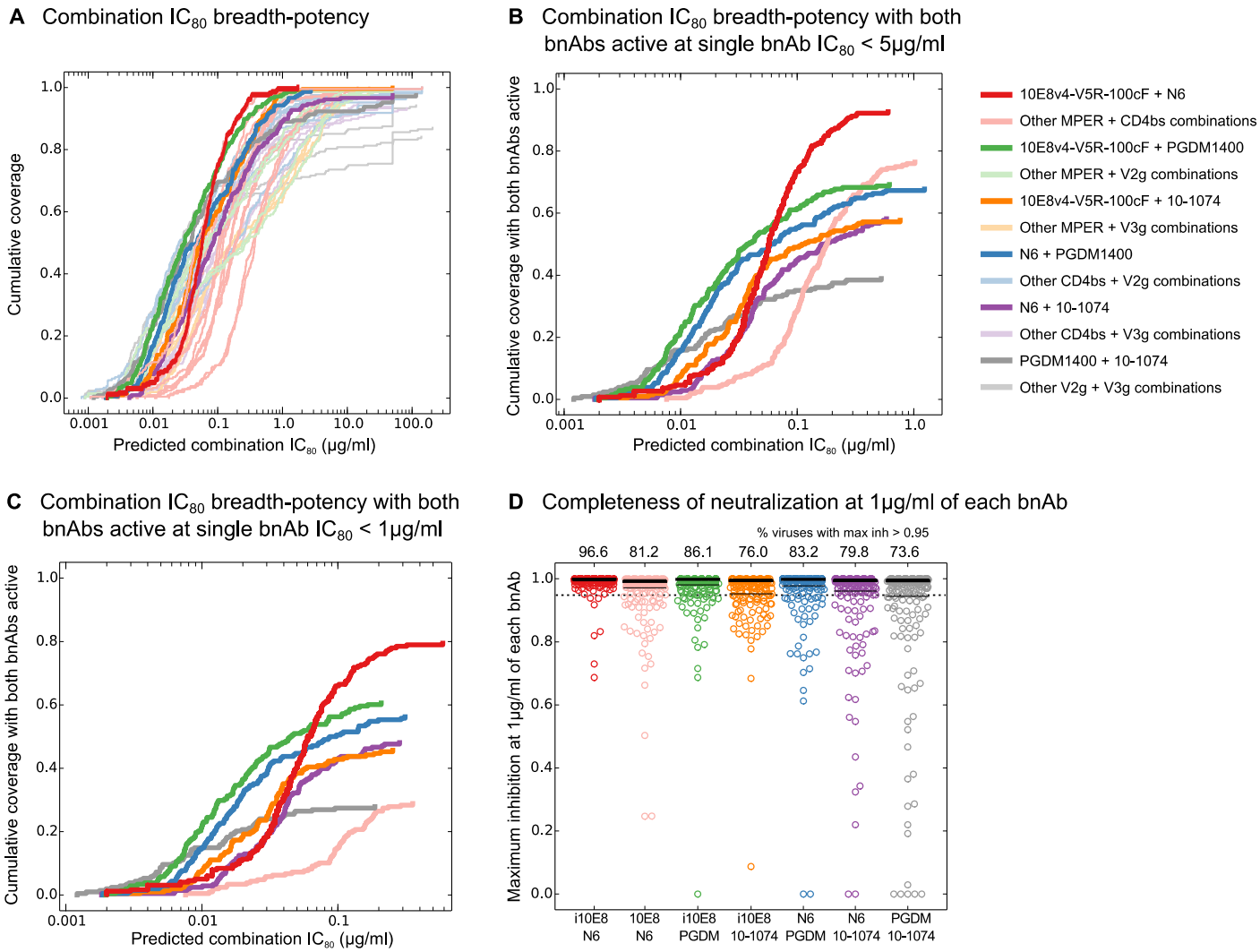

Figure S5. Predicted neutralization for antibody combinations, including those with 10E8v4-5R+100cF. Related to Figure 7. (**A**) IC_{80} breadth potency curve for 2 bnAb combinations. Each combination is assumed to have equal concentrations of each bnAb and combination IC_{80} is the concentration of each bnAb for 80% neutralization of a given virus. Bold, dark lines show data for the best-in-class combinations, and thin, faint lines show data for other combinations from the same class. Experimental IC_{80} data is shown for the combination of 10E8v4-5R+100cF with N6. (**B**) IC_{80} breadth-potency curves with both bnAbs active at single bnAb IC_{80} < 5 µg/ml. The cumulative coverage is plotted versus combination IC_{80} considering only those viruses neutralized by both bnAbs. A virus was considered neutralized by a bnAb if individual bnAb IC_{80} < 5 µg/ml. The pink curve shows coverage with both bnAbs active for 10E8 + N6. Experimental IC_{80} data is shown for the combination of 10E8v4-5R+100cF with N6. (**C**) Same as B using activity threshold of single bnAb IC_{80} < 1 µg/ml. (**D**) Predicted completeness of neutralization for antibody combinations at 1µg/ml of each bnAb. The numbers on top indicate the percent viruses that were predicted to be neutralized at >95%.

Table S2. Crystallographic data and refinement. Related to Figure 1.

	10E8v4-5R+100cF Fab:gp41 peptide
PDB accession code	5WDF
Data collection	
Space group	*P*1
Cell constants	
a, *b*, *c* (Å)	57.2 60.9, 70.1
α, β, γ (°)	103.0, 107.4, 100.0
Unique reflections	14,534
Wavelength (Å)	1.00
Resolution (Å)	50.0-3.1 (3.15-3.10)*
R_{merge}	11.1 (48.4)
R_{pim}	7.9 (36.7)
$CC_{1/2}$	0.915 (0.715)
$I / \sigma I$	11.0 (2.1)
Completeness (%)	93.2 (83.6)
Redundancy	2.6 (2.0)
Refinement	
Resolution (Å)	45.1-3.1
Reflections used in refinement	14,394
R_{work} / R_{free} (%)	24.6/28.1
No. atoms	
Protein	6,558
B-factors (Å^2)	
Protein	114
R.m.s. deviations	
Bond lengths (Å)	0.002
Bond angles (°)	0.605
Ramachandran	
Favored regions (%)	95.3
Allowed regions (%)	4.42
Disallowed regions (%)	0.25

* Values in parentheses are for highest-resolution shell.